

Banner appropriate to article type will appear here in typeset article

# Experimental and theoretical investigation of drag loads on side-by-side flexible blades in a uniform current

Zhilong Wei<sup>1,2</sup>, Trygve Kristiansen<sup>2</sup>, David Kristiansen<sup>2</sup>, and Yanlin Shao<sup>1</sup>†

<sup>1</sup>Department of Civil and Mechanical Engineering, Technical University of Denmark, Kgs. Lyngby, 2800, Denmark

<sup>2</sup>Department of Marine Technology, Norwegian University of Science and Technology, Trondheim, 7491, Norway

This study investigates the hydrodynamic drag force on side-by-side flexible blades in a uniform current through experimental and theoretical approaches. Four silicone rubber blade models with varying dimensions were arranged in side-by-side bunches and tested in a circulating water tunnel. The experiments cover the static regime and the flutter regime. We examine four non-dimensional parameters to assess their effects on the bulk drag coefficient  $C_{D,\text{bulk}}$  and the onset of flutter: the drag-to-stiffness ratio  $Ca$ , the buoyancy-to-stiffness ratio  $B$ , the mass ratio of fluid inertia to total system inertia  $\beta$ , and the slenderness parameter  $\lambda$ . The results show that  $C_{D,\text{bulk}}$  decreases in the static regime with the rate of decrease closely related to  $B$  starting at  $Ca/B > O(1)$ , and settles to an almost constant value in the flutter regime. Increasing  $\beta$ ,  $B$ , or  $\lambda$  delays the onset of flutter. By introducing the equivalent thickness and bending stiffness, existing theoretical models for individual blades are utilized to predict the drag reduction of side-by-side blade assemblies. The analytical model accurately predicts drag reduction in the static regime, while the numerical model predicts both the onset of flutter and drag reduction in both regimes when appropriate cross-flow hydrodynamic coefficients are applied. Meanwhile, we investigate the reactive force model term by term to identify their impact on the system stability and drag reduction, demonstrating its superiority over the traditional Morison's equation for highly compliant blades in cross flows.

**Key words:** flow-structure interactions, slender-body theory

## 1. Introduction

Flexible structures subjected to transverse flows are pushed to align with the flow direction, and the drag they experience is modified by the deformation. Vogel (1996) suggested the use of the term *reconfiguration* when dealing with biological structures to emphasize the strategy of being flexible to reduce the drag. Seaweeds are one of the most common examples. In the case of cultivated seaweeds, to maximize the yield, the seaweed blades usually grow densely

† Email address for correspondence: yshao@dtu.dk

side by side on longlines (Grebe *et al.* 2019; Campbell *et al.* 2019; Zhu *et al.* 2021) instead of being separated from each other.

The theory of static reconfiguration and drag reduction of an individual flexible blade in a steady background flow is well established. Gosselin *et al.* (2010) introduced the reconfiguration number to quantify the drag reduction in their wind tunnel experiments on flexible rectangular plates and cut disks. They developed a simple analytical model based on a force balance between drag and bending stiffness, which predicted well the observed drag reduction. Luhar & Nepf (2011) incorporated the gravity and buoyancy and used the effective length to represent drag reduction. Both concepts (reconfiguration number and effective length) have been widely used since then, for example, the former in Henriquez & Barrero-Gil (2014); Whittaker *et al.* (2015); Leclercq *et al.* (2018); Baskaran *et al.* (2023), and the latter in Lei *et al.* (2021); Sun *et al.* (2024). However, the relationship between them has not been clarified.

Flexible blades exposed to a transverse flow tend to be increasingly aligned with the flow direction. At a certain flow speed flutter occurs, a dynamic instability resulting from the competition between reactive fluid forces and structural stiffness (Leclercq *et al.* 2018). The analytical models mentioned above are no longer applicable in this dynamic regime. Leclercq *et al.* (2018) developed a numerical model to study drag reduction in the flutter regime and concluded that while flutter does not prevent drag reduction compared to rigid structures, it decreases the extent to which the drag of flexible structures is reduced. In other words, after flutter occurs, the drag is not reduced as rapidly as in the static regime. Boukor *et al.* (2024) reached a similar conclusion from their experiments, referring to this phenomenon as the flutter limitation of drag reduction. It is unknown whether this limitation exists in the scenario of side-by-side blades and, if so, how it differs from that of an individual blade.

Studies on the hydrodynamic drag of side-by-side flexible blade bunches are relatively scarce in the literature. Buck & Buchholz (2005) conducted towing tests on individual blades of wild and cultivated *Laminaria saccharina*, as well as on bunches of laminarians. For cultivated algae from an exposed offshore farm, the kelp blades were flat and narrow, and the reported drag coefficient initially decreased with increasing current velocity before reaching some constant values with the current velocity, as shown in their Figure 7. Fredriksson *et al.* (2020) performed towing tests on a dense aggregate of artificial kelp blades and reported drag-area values. Lei *et al.* (2021) observed that the drag increased with velocity at a rate less than quadratic in towing tests on dense aggregates of cultivated *Saccharina latissima*. However, the existing studies based on model tests do not present systematic analysis utilizing governing non-dimensional parameters to unravel the physics.

When multiple flexible blades are arranged in bunches, their interactions with the flow and with each other introduce additional complexities absent in isolated blades. Studies have found that the drag on a bunch is less than the sum of the individual drag forces (Carrington 1990; Johnson 2001; Buck & Buchholz 2005). The relationship between the drag on a bunch and that on an individual blade is not clearly understood, let alone the drag on side-by-side bunches. As mentioned earlier, well-developed theoretical models exist for an individual blade in an infinite fluid domain. If these models can be moderately modified to study the drag load on side-by-side blade bunches, there would be no need to develop complex three-dimensional models.

The first objective of this paper is to calibrate the bulk drag coefficients for side-by-side blades in a current, using comprehensive experimental data that spans both the static and flutter regimes. Leveraging this data set, the study reexamines key non-dimensional parameters to analyze their influence on the bulk drag coefficient in both regimes and on the initiation of flutter. Additionally, the paper aims to assess whether established analytical and numerical models for individual blades can accurately capture drag loads in side-by-side

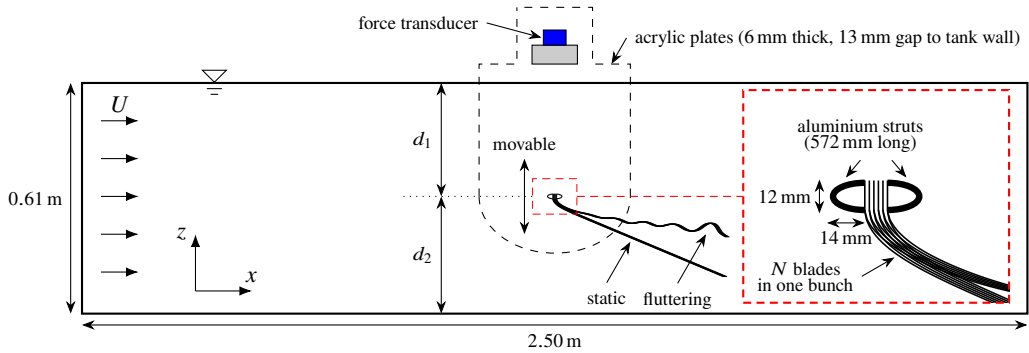


Figure 1: Side view sketch of the test section and setup in the Circulating Water Tunnel (CWT) at NTNU.

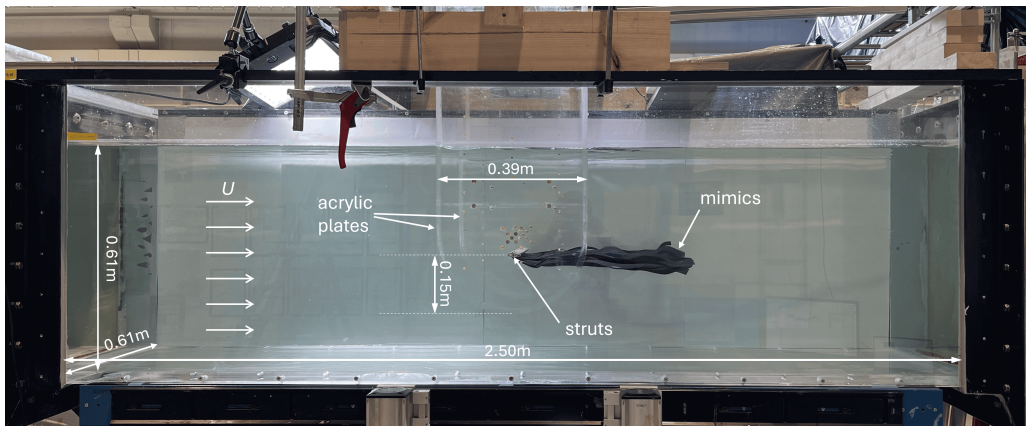


Figure 2: Photo of the test section of the CWT at NTNU and the experimental setup.

blade configurations. Furthermore, the reactive force model will be scrutinized term by term to evaluate its impact on drag reduction and system stability. Finally, we seek to determine whether the traditional Morison's equation is adequate for scenarios involving highly flexible blades in cross-flow conditions.

The paper is organized as follows. In § 2, we describe the experimental setup and procedures. § 3 presents the development of the analytical model and provides a brief introduction to the numerical model, along with a discussion of their limitations. In § 4, the experimental results are presented using non-dimensional parameters, and the effects of these parameters are analyzed. In § 5, we assess the capability of the two theoretical models by comparing their predictions with the experimental data and dive into the hydrodynamic load model, especially the reactive force to see contribution from different terms to the drag reduction and system stability. Conclusions are provided in § 6.

## 2. Experiments

The experiments were performed in the Circulating Water Tunnel (CWT) at the Norwegian University of Science and Technology (NTNU) in Trondheim. An illustration of the test setup is provided in figure 1 and figure 2. The test section of the CWT is 2.50 m long, 0.61 m wide, and 0.61 m deep.

The blade mimics were clamped at the top end between a pair of aluminum struts positioned

Mimic	Length $l$ (m)	Width $b$ (mm)	Thickness $d$ (mm)	Aspect ratio $l/b$	number of bunches
1	0.5	26.2	0.5	19.1	22
2	0.5	52.4	0.5	9.5	11
3	0.5	115.2	0.5	4.3	5
4	0.5	52.4	1.0	9.5	11

Table 1: Dimensions of the four blade mimics.

in the middle of the tank. The struts were cut from a 572 mm long cylinder with an elliptical cross-section, featuring a semi-major axis of 14 mm and a semi-minor axis of 6 mm. These struts were fixed to two side acrylic plates, with their edges streamlined to minimize drag. A rig connected the two plates at the top, where a six degree-of-freedom force transducer was mounted. Measurements were sampled at a rate of 200 Hz.

Sets of four different blade mimics with rectangular cross-sections were fabricated from silicone rubber sheets, with a density of  $\rho_s = (1264.5 \pm 66.0) \text{ kg/m}^3$  and the Young's modulus of  $E = (5.36 \pm 0.40) \text{ MPa}$ . The density was calculated from measured mass and volume of sample material, while Young's modulus was measured using Peirce's testing apparatus (Peirce 1930). The dimensions of the four mimics are provided in table 1. All four mimic types had the same length. Mimics 1, 2, and 3 shared the same thickness but differed in width, while Mimics 2 and 4 had the same width but differed in thickness. By width we refer to the direction across the tank ( $y$ -axis), as illustrated in figure 3.

Along the struts, several blade bunches were placed side by side, as shown in table 1 and figure 3c. Within each bunch, a number of blades ( $N = 10, 5, 2, 1$ ) with the same shape were overlapped on top of one another (see the magnified window in figure 1). This arrangement allowed us to study the effect of line density, i.e., the number of blades per unit length.

A total of eleven current speeds,  $U = 0.050, 0.067, 0.091, 0.122, 0.164, 0.221, 0.297, 0.400, 0.538, 0.725, \text{ and } 0.975 \text{ m/s}$  were studied. The speeds were spaced evenly on a logarithmic scale. Note that the actual current speed  $U$  might deviate slightly from the target speeds mentioned above. The flow speeds used for analysis were calibrated based on the pump rotation frequency, and this calibration was performed prior to the tests. The CWT is equipped with a honeycomb flow straightener and a contraction before the test section to suppress turbulence intensity to around 1% of the inflow (without model). The frame (including the struts and the acrylic plates) holding the blades was vertically adjustable. For each combination of flow speed and blade mimic, the submergence  $d_1$  of the struts and the distance  $d_2$  to the tank bottom were adjusted to ensure that the blade tip would not touch the bottom and the blades would remain as far from the free surface as possible, to minimize free-surface effects. The possible submergence depths were  $d_1 = 30, 26, 22, 18, 14$  and 10 cm. In some cases, tests were performed at multiple submergence depths.

For each combination of current speed and blade mimic, three repeated tests were conducted. Each repetition involved a 5 min test, with the middle 3 min time window used for analysis. The loads on the frame alone were measured in the same manner for the eleven flow speeds at all submergence depths, without the model blades. These baseline loads were then subtracted from the corresponding tests with the model blades.

### 3. Analytical and numerical models

In this section, we first examine the motion of an individual flexible blade confined to a two-dimensional plane in infinite fluid and identify the key non-dimensional parameters. We then introduce the concepts of equivalent thickness and bending stiffness for a collection

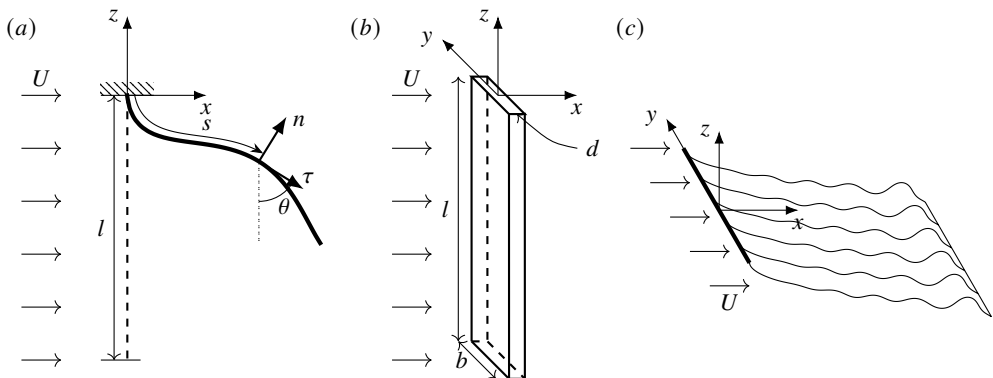


Figure 3: (a) Side view of the deformed blade subjected to a uniform flow  $U$  in the  $x$ -direction. (b) The undeformed blade has dimensions  $l \times b \times d$ . (c) 3D sketch of the deformed blades side-by-side.

of overlapping blades. Afterward, we provide a brief introduction to the numerical model used to simulate all the experimental cases. From this point forward, both the analytical and numerical models will be collectively referred to as theoretical models. Finally, we discuss the limitations of the applied theoretical models.

### 3.1. Analytical model

We consider a flexible blade with constant length  $l$ , width  $b$ , and thickness  $d$ , clamped at one end and initially oriented perpendicular to a uniform, steady flow  $U$  of fluid with density  $\rho$ , as shown in figure 3. The blade is assumed to be thin, i.e.,  $b \gg d$ , and its motion is confined to the  $xz$ -plane. We also assume that the structure, characterized by density  $\rho_s$  and bending stiffness  $EI$ , is slender ( $l \gg b$ ), and the two-dimensional inextensible Euler-Bernoulli beam model adequately represents the effect of bending.

As shown in figure 3a, a curvilinear coordinate  $s$  is defined to denote the arc length along the blade from the base. The position vector  $\mathbf{r} = x(s, t)\mathbf{e}_x + z(s, t)\mathbf{e}_z$  is a function of both  $s$  and time  $t$ .  $\theta$  is the local angle between the tangent vector  $\boldsymbol{\tau} = \partial\mathbf{r}/\partial s$  and  $-\mathbf{e}_z$ . Additionally,  $\mathbf{n}$  is the normal vector. In the following, we loosely follow Leclercq *et al.* (2018) to derive the governing equation of motion for a flexible blade, with the exception that the blade is not assumed as neutrally buoyant.

The force balance on an infinitesimal segment leads to

$$\mu \frac{\partial^2 \mathbf{r}}{\partial t^2} = \frac{\partial \mathbf{F}}{\partial s} + \mathbf{q} + \mathbf{B}, \quad (3.1)$$

where  $\mu = \rho_s b d$  is the body mass per unit length,  $\mathbf{q}$  is the external distributed hydrodynamic load on the body,  $\mathbf{B} = -(\rho_s - \rho)g b d \mathbf{e}_z$  is the effective weight in fluid per unit length, and  $\mathbf{F} = T\boldsymbol{\tau} + Q\mathbf{n}$  is the internal force.  $T$  and  $Q$  are the tension and shear force, respectively.  $g$  is the acceleration of gravity. The bending moment  $M$  is related to the curvature  $\kappa = \partial\theta/\partial s$  by  $M = EI\kappa$ . The shear force  $Q$  is given by  $Q = -\partial M/\partial s = -EI\partial\kappa/\partial s$ . The boundary conditions are  $x = z = \theta = 0$  at the clamped base  $s = 0$  and  $T = M = Q = 0$  at the free tip  $s = l$ .

Let  $\mathbf{U} = U\mathbf{e}_x$  be the flow velocity vector. The relative velocity between the ambient flow and the structure can be decomposed along the blade tangential vector  $\boldsymbol{\tau}$  and the blade normal

vector  $\mathbf{n}$  as

$$U_\tau = \left( \frac{\partial \mathbf{r}}{\partial t} - \mathbf{U} \right) \cdot \boldsymbol{\tau}, \quad U_n = \left( \frac{\partial \mathbf{r}}{\partial t} - \mathbf{U} \right) \cdot \mathbf{n}. \quad (3.2)$$

Following Leclercq & de Langre (2018) and Leclercq *et al.* (2018), the distributed hydrodynamic load  $\mathbf{q}$  on the body consists of two parts, the resistive drag

$$\mathbf{q}_d = -\frac{1}{2} \rho C_D b |U_n| U_n \mathbf{n}, \quad (3.3)$$

and the reactive force (Lighthill 1971; Candelier *et al.* 2011)

$$\mathbf{q}_{am} = -m_a \left[ \frac{\partial(U_n \mathbf{n})}{\partial t} - \frac{\partial(U_\tau U_n \mathbf{n})}{\partial s} + \frac{1}{2} \frac{\partial(U_n^2 \boldsymbol{\tau})}{\partial s} \right], \quad (3.4)$$

where  $m_a = \pi \rho C_M b^2 / 4$  is the added mass. Here,  $C_D$  and  $C_M$  are the cross-flow drag coefficient and added mass coefficient, respectively. It should be noted that in Leclercq & de Langre (2018) and Leclercq *et al.* (2018),  $C_M = 1$  is universally assumed. For an inextensible structure, (3.4) simplifies to

$$\mathbf{q}_{am} = -m_a \left[ \frac{\partial^2 \mathbf{r}}{\partial t^2} \cdot \mathbf{n} - 2 \frac{\partial \theta}{\partial t} U_\tau + \kappa \left( U_\tau^2 - \frac{1}{2} U_n^2 \right) \right] \mathbf{n}. \quad (3.5)$$

For a detailed derivation, refer to Appendix A of Leclercq *et al.* (2018). The Froude-Krylov force is here neglected since the blade is assumed to be thin.

Using the relation between the bending moment  $M$  and the shear force  $Q$ , (3.1) becomes

$$\mu \frac{\partial^2 \mathbf{r}}{\partial t^2} = \frac{\partial}{\partial s} \left( T + \frac{1}{2} EI \kappa^2 \right) \boldsymbol{\tau} + \left( \kappa T - EI \frac{\partial^2 \kappa}{\partial s^2} \right) \mathbf{n} + \mathbf{q}_d + \mathbf{q}_{am} + \mathbf{B}. \quad (3.6)$$

After projection on the tangential and normal vectors and eliminating the unknown tension  $T$ , we obtain the governing equation of motion for a flexible blade:

$$\begin{aligned} (\mu + m_a) \frac{\partial^2 \mathbf{r}}{\partial t^2} \cdot \mathbf{n} - \mu \kappa \int_l^s \frac{\partial^2 \mathbf{r}}{\partial t^2} \cdot \boldsymbol{\tau} ds + EI \left( \frac{\partial^2 \kappa}{\partial s^2} + \frac{1}{2} \kappa^3 \right) \\ + m_a \left[ \kappa \left( U_\tau^2 - \frac{1}{2} U_n^2 \right) - 2 U_\tau \frac{\partial \theta}{\partial t} \right] + \frac{1}{2} \rho C_D b |U_n| U_n + (\rho_s - \rho) g b d \left( \kappa \int_l^s \cos \theta ds + \sin \theta \right) = 0. \end{aligned} \quad (3.7)$$

Following Leclercq *et al.* (2018), (3.7) is made non-dimensional using the blade length  $l$  and the first natural period of the structure in small-amplitude oscillations in the fluid  $T_n = l^2 \sqrt{(\mu + m_a) / EI}$ . The non-dimensional form is

$$\begin{aligned} \frac{\partial^2 \tilde{\mathbf{r}}}{\partial \tilde{t}^2} \cdot \mathbf{n} - (1 - \beta) \tilde{\kappa} \int_1^{\tilde{s}} \frac{\partial^2 \tilde{\mathbf{r}}}{\partial \tilde{t}^2} \cdot \boldsymbol{\tau} d\tilde{s} + \frac{\partial^2 \tilde{\kappa}}{\partial \tilde{s}^2} + \frac{1}{2} \tilde{\kappa}^3 \\ + \beta \left[ \tilde{\kappa} \left( \tilde{U}_\tau^2 - \frac{1}{2} \tilde{U}_n^2 \right) - 2 \tilde{U}_\tau \frac{\partial \theta}{\partial \tilde{t}} \right] + \beta \lambda |\tilde{U}_n| \tilde{U}_n + \mathbf{B} \left( \tilde{\kappa} \int_1^{\tilde{s}} \cos \theta d\tilde{s} + \sin \theta \right) = 0, \end{aligned} \quad (3.8)$$

where the tilde ( $\tilde{\cdot}$ ) denotes non-dimensional variables. The boundary conditions are  $\tilde{\mathbf{r}} = \mathbf{0}$  and  $\theta = 0$  at  $\tilde{s} = 0$  and  $\tilde{\kappa} = \partial \tilde{\kappa} / \partial \tilde{s} = 0$  at  $\tilde{s} = 1$ . The non-dimensional relative velocity is given by  $\tilde{U}_n \mathbf{n} + \tilde{U}_\tau \boldsymbol{\tau} = \partial \tilde{\mathbf{r}} / \partial \tilde{t} - \mathbf{u} / \sqrt{\beta} \mathbf{e}_x$ , where  $\mathbf{u} = \sqrt{Ca} / \lambda$  is the reduced velocity.

The system is governed by four non-dimensional parameters:

$$\beta = \frac{m_a}{\mu + m_a}, \quad Ca = \frac{1}{2} \frac{\rho C_D b U^2 l^3}{EI}, \quad \mathbf{B} = \frac{(\rho_s - \rho) g b d l^3}{EI}, \quad \text{and} \quad \lambda = \frac{\rho C_D b l}{2 m_a} = \frac{2}{\pi} \frac{C_D}{C_M} \frac{l}{b}. \quad (3.9)$$

Physically, the mass ratio  $\beta$  represents the proportion of fluid inertia relative to the total inertia of the system. When the blades are quite thin, i.e.,  $d \ll b$ ,  $\beta \rightarrow 1$ . The Cauchy number  $Ca$  represents the ratio of the drag force to the restoring force due to bending stiffness. Although  $Ca$  does not explicitly appear in (3.8), it is incorporated through the reduced velocity  $u = \sqrt{Ca/\lambda}$ . The buoyancy parameter  $B$  indicates the ratio of the restoring force due to buoyancy to that due to bending stiffness. For neutrally buoyant structures,  $B = 0$ , and (3.8) reduces to the form presented by Leclercq *et al.* (2018). We note that we refer to  $B$  as the buoyancy parameter following Lei & Nepf (2019b) and Vettori *et al.* (2024); however, in this study, the structure's density is greater than that of water. The slenderness parameter  $\lambda$  is proportional to the aspect ratio  $l/b$  and can be interpreted as the ratio of the resistive drag to the reactive force.

We can examine the four non-dimensional parameters from the underlying physical problem of a flexible rectangular blade deflected in an infinite fluid domain. Nine quantities are to be taken into consideration as follows:

- three dimensions of the blade, the length  $l$  [m], the width  $b$  [m], and the thickness  $d$  [m]
- two mechanical properties of the blade, its density  $\rho_s$  [ $\text{kg m}^{-3}$ ] and its Young's modulus  $E$  [ $\text{N m}^{-2}$ ]
- current speed  $U$  [ $\text{m s}^{-1}$ ]
- fluid density  $\rho$  [ $\text{kg m}^{-3}$ ], fluid kinematic viscosity  $\nu$  [ $\text{m}^2 \text{s}^{-1}$ ]
- gravitational acceleration  $g$  [ $\text{m s}^{-2}$ ]

According to the  $\Pi$  theorem of Buckingham (1914), the problem can be described by six non-dimensional parameters. However, since we assume that the blades are very thin (i.e.,  $d \ll b$ ), the thickness-to-width ratio  $d/b$  is within narrow range and has minimal impact. Additionally, the fluid viscosity  $\nu$ , which is usually associated with the Reynolds number  $Re$ , does not significantly influence drag for a plate in cross flow. Consequently, we can exclude these two parameters, leaving four non-dimensional parameters that sufficiently describe the physical problem.

In the experiments, one or multiple layers of blades were arranged in each bunch. The blades were neatly overlapped on one another and, although not physically adhered, they behaved similarly. As a first approximation, when studying a bunch of blades, we treat the blades as a single unit and apply the same theory from § 3.1, but with the blade thickness  $d$  replaced by  $Nd$  and the bending stiffness  $EI$  replaced by  $NEI$ , where  $N$  is the number of overlapping blades in one bunch.  $Nd$  and  $NEI$  are referred to as the equivalent thickness and equivalent bending stiffness of the bunch of blades. According to (3.9), given the same values of  $C_D$  and  $C_M$ , for a bunch consisting of  $N$  blades, the buoyancy parameter  $B$  and the slenderness parameter  $\lambda$  are identical to those of an individual blade within that bunch. The Cauchy number  $Ca$  is reduced to  $1/N$  of that for an individual blade due to the increased bending stiffness  $EI$ , and the mass ratio  $\beta$  decreases slightly as  $\mu$  increases to  $N\mu$  and  $m_a$  remains unchanged (assume the same  $C_M$ ).

### 3.2. Numerical model

Unlike Leclercq *et al.* (2018), who solved the full time-dependent nonlinear (3.8) using an implicit time-stepping method, we employ an explicit truss-spring model (Wei *et al.* 2024) to investigate the blade reconfiguration and drag loads. This numerical structural model utilizes the same load model (equations (3.3) and (3.4)) as Leclercq *et al.* (2018), with the key difference that the structure is stretchable and the tension is derived from the constitutive law, i.e., Hook's law, rather than being treated as an unknown due to the inextensibility condition. Additionally, our numerical model solves the two-dimensional governing equation of motion (3.6) instead of (3.8). Our model has been validated against the experiments by Leclercq &



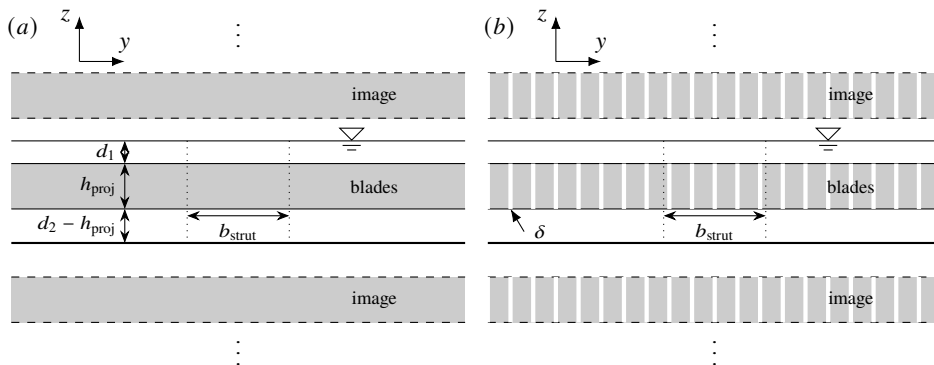


Figure 4: (a) The blades extended in the  $y$ -direction and its images about the free surface and the tank bottom. (b) Gaps between adjacent bunches of blades.

de Langre (2018) on the reconfiguration of elastic blades in oscillatory flow, see details in Wei *et al.* (2024). The model is applied to simulate all our experimental cases. The same strategy of equivalent thickness and bending stiffness introduced in § 3.1 is used in the numerical simulations. Each blade is discretized into 120 equal-length segments and the time step size is  $1 \times 10^{-5}$  s. The computations are carried on for 45 s with the last 5 s time window used for analysis.

### 3.3. Limitations of the theoretical models

Some assumptions made in the analytical and numerical models are not entirely consistent with the experiments, such as the fluid domain, the assumption of pure in-plane motion, synchronous motions, and the absence of struts.

Firstly, both the analytical and numerical models assume an individual blade situated in an infinite fluid domain, where the incoming flow passes around all four edges of the blade. For slender blades, i.e.,  $l/b \gg 1$ , flow separation at the side edges contributes more significantly to the total loads than at the tip edges. However, in the experiments, the blades were arranged side by side in a tank with limited cross-span. The free-surface elevation due to the presence of the model is small and can be neglected. By mirroring the setup about the free surface and the tank bottom, and extending it along the  $y$ -direction, the physical problem effectively becomes one of flow around parallel patches of blades, as illustrated in figure 4a.

Additionally, due to three-dimensional motions or asynchronous movements, the blade bunches in the experiments were not perfectly aligned with each other. This misalignment resulted in gaps between the bunches, allowing some flow to pass around the side edges, as shown in figure 4b. The theoretical models can still capture the essential physics of the system, although  $C_D$  and  $C_M$  of the blade patches may deviate from those for a rigid plate in an infinite fluid domain.

Moreover, both theoretical models assume that blade motion is confined to the  $xz$ -plane. In contrast, the blades in the experiments exhibited three-dimensional motions, including twisting around their longitudinal axes. Blades at the far ends of the struts were sometimes drawn toward the adjacent acrylic plates.

The theoretical models use equivalent thickness and equivalent bending stiffness to represent multiple overlapping blades as a single unit. This approach neglects the interactions between individual blades within a bunch and their asynchronous movements. In the experiments, adjacent blades could also interact directly through collisions or by hydrodynamic



---

Mimic	$\beta$	Ca	B	$\lambda$
1	[0.765, 0.970]	$[5.46 \times 10^2, 2.08 \times 10^6]$	2904.6	23.7
2	[0.867, 0.985]	$[5.46 \times 10^2, 2.08 \times 10^6]$	2904.6	11.8
3	[0.935, 0.993]	$[5.46 \times 10^2, 2.08 \times 10^6]$	2904.6	5.4
4	[0.765, 0.970]	$[6.28 \times 10^1, 2.59 \times 10^5]$	726.1	11.8

---

Table 2: Values or ranges of the non-dimensional parameters.

---

interaction. While these interactions are not directly captured in the models, they might be incorporated through the coefficients  $C_D$  and  $C_M$ .

Finally, although the struts used in the tests were streamlined, they might still have induced flow separation and altered the downstream flow, especially at large Ca, where the blades were nearly aligned horizontally and positioned directly behind the struts. The presence and influence of the struts are not accounted for in either model.

#### 4. Experimental results

In this section, the experimental results are presented using non-dimensional parameters. In the definition of the four non-dimensional parameters in § 3.1,  $C_D$  and  $C_M$  are actually unknown and not likely to be directly calibrated from the experiments. Following Luhar & Nepf (2011), we assume  $C_D = 1.95$ , unless stated otherwise. This is within values established for flat plates in steady flows in the literature. The value of  $C_M$  will be specified whenever it is used in the subsequent analysis. The values or range of the four non-dimensional parameters covered in the experiments are listed in table 2. When calculating  $\beta$  and  $\lambda$  in the table, we assume  $C_M = 1$ . The mean values for the material properties,  $\rho_s = 1264.5 \text{ kg/m}^3$  and  $E = 5.36 \text{ MPa}$ , are used. For each blade mimic, tests were conducted at eleven different current speeds, with  $N = 1, 2, 5$ , or 10 blades in each bunch.

##### 4.1. Static reconfiguration and flutter

Two distinct reconfiguration regimes were observed in the experiments. At low values of Ca, the blades were deflected in the direction of the flow and settled into a static position. As Ca increased, the blades became more aligned with the horizontal plane. At certain critical values of Ca, flutter was observed to initiate from the blade tip. As Ca continued to increase, the flutter propagated towards the root, eventually covering most of the blade length. Example photographs of the static reconfiguration and flutter are shown in figure 5. Several videos recorded during the experiments are also available in the supplementary material.

##### 4.2. Bulk drag coefficient

In practical applications, the primary concern is the hydrodynamic loads acting on the blades. The bulk drag coefficient  $C_{D,\text{bulk}}$  (Vogel 1989; Kobayashi *et al.* 1993) can be calculated from the measured mean horizontal force  $\bar{F}$  using the following expression:

$$C_{D,\text{bulk}} = \frac{\bar{F}}{1/2\rho b_{\text{strut}}U^2l}, \quad (4.1)$$

where  $b_{\text{strut}} = 576 \text{ mm}$  is the strut length, or total width of the blades, not accounting for gaps  $\delta$  between the blades. The concept of the bulk drag coefficient is practical in engineering applications. Once calibrated, it can be used to estimate the drag force based on blade

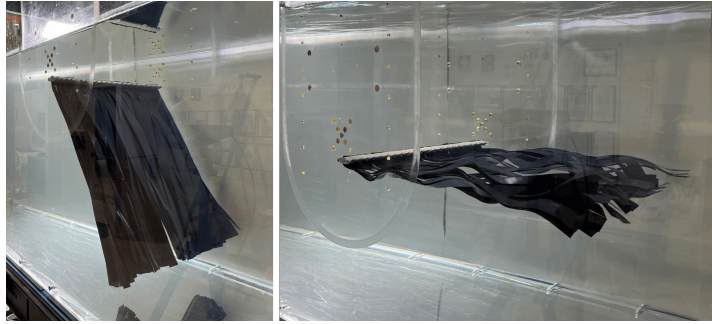


Figure 5: The static reconfiguration at  $Ca = 9.80 \times 10^2$  (left) and flutter at  $Ca = 5.33 \times 10^4$  (right) of Mimic 1.

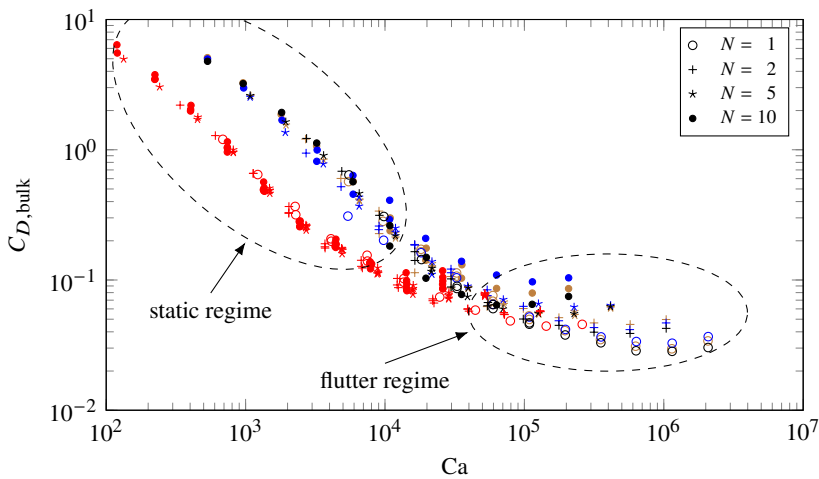


Figure 6: The calibrated  $C_{D,bulk}$  from the experiments versus  $Ca$ . Mimic 1–4 are respectively represented in brown, blue, black, and red. The number of blade per bunch  $N$  is represented by different markers: circle  $\circ$ ,  $N = 1$ ; plus  $+$ ,  $N = 2$ ; five-pointed star  $\star$ ,  $N = 5$ ; dot  $\bullet$ ,  $N = 10$ .

dimensions and the ambient current speed. The calibrated values of  $C_{D,bulk}$  from 303 tests are plotted in figure 6. Error bars have been omitted in this figure for clarity. The uncertainty analysis is provided in appendix A.

$C_{D,bulk}$  exhibits different behavior in the static and flutter regimes. In the static regime,  $C_{D,bulk}$  monotonically decreases with increasing flow speed. Around the critical  $Ca$ , where flutter occurs, a noticeable change is observed. In the flutter regime,  $C_{D,bulk}$  becomes nearly constant. This general trend aligns with the findings reported by Buck & Buchholz (2005). At small  $Ca$  within ranges  $[1 \times 10^2, 2 \times 10^3]$ , some  $C_{D,bulk}$  values exceed  $C_D = 1.95$ . As discussed in § 3.3, the limited fluid domain due to the presence of the free surface and the tank floor and significant blockage effect contribute to this observation. The blockage effect is further investigated in § 5.2. In this section, we discuss the effects of the non-dimensional parameters.

The effect of  $l/b$  instead of  $\lambda$  is discussed because  $l/b$  is fixed and known, whereas  $\lambda$  depends on unknown  $C_D$  and  $C_M$ . Mimic 1, 2, and 3 share the same buoyancy parameter and differ in the aspect ratio, see table 1 and table 2. As shown in figure 7, varying the aspect ratio has in general small effect on  $C_{D,bulk}$  in both regimes, nor does it significantly affect

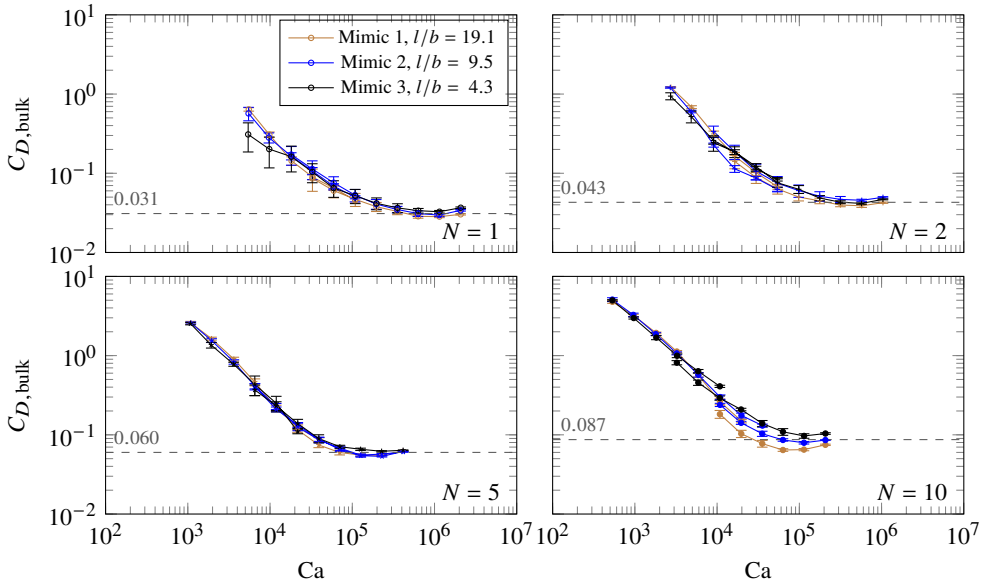


Figure 7: Effect of the aspect ratio  $l/b$  on  $C_{D,\text{bulk}}$  for Mimics 1–3 of the same  $B$  with different numbers of blades per bunch ( $N$ ). The dashed horizontal lines denotes the average  $C_{D,\text{bulk}}$  in the flutter regime from the three mimics with varying aspect ratios.

the critical  $Ca$ . The discrepancies observed among different mimics at  $N = 10$  arise because the tests were conducted at varying submergence depths. This was done to prevent the blades from touching the tank bottom and to minimize the effects of the free surface. This finding contrasts with the conclusions drawn for individual blades by Leclercq *et al.* (2018). In their numerical study, both  $C_D$  and  $C_M$  were fixed, allowing  $l/b$  to effectively represent  $\lambda$ . They found that elongation stabilized the system. The more slender the structure, the higher the critical  $Ca$  required for flutter onset. As discussed in § 3.3, models developed for individual blades may not accurately represent the behavior of side-by-side blades.

Mimic 2 and Mimic 4 share the same  $l/b$  but differ in  $B$ . As demonstrated in figure 8, in the static regime, a larger  $B$  results in a higher  $C_{D,\text{bulk}}$ , as the effective weight  $B$  pulls the blades downward, increasing the projected area against the flow.  $B$ , as a restoring force, stabilizes the system by delaying the onset of flutter. By delay, it means the flutter occurs at a higher  $Ca$ . If the structural density is less than that of water,  $B$  becomes negative, which destabilizes the system.

When the number of blades in a bunch is increased,  $B$  and  $l/b$  remain unchanged. However, since  $C_M$  appears in both  $\beta$  and  $\lambda$ , and  $C_D$  is included in  $\lambda$  as well, it becomes challenging to isolate the effects of  $N$  on  $C_D$  and  $C_M$ , and subsequently to assess the impact of  $\beta$  on  $C_{D,\text{bulk}}$ . The interplay between these parameters complicates a direct evaluation of how increasing the number of blades affects the overall drag coefficient. Nevertheless, increasing  $N$  should reduce  $\beta$ . In other words, as the body mass increases with more blades in a bunch, the proportion of the fluid inertia in the system decreases.

Observations (figure 9) indicate that the effect of  $\beta$  on  $C_{D,\text{bulk}}$  in the static regime is minor for all four mimics. This is because  $\beta$  only appears in the unsteady terms in (3.8). In the static regime, where all time derivatives vanish, the governing equations become independent on  $\beta$ . However,  $\beta$  does have a stabilizing effect and thus a larger  $\beta$  leads to a higher critical  $Ca$  where flutter starts to develop.

In conclusion, the effects of the non-dimensional parameters on  $C_{D,\text{bulk}}$  in both regimes

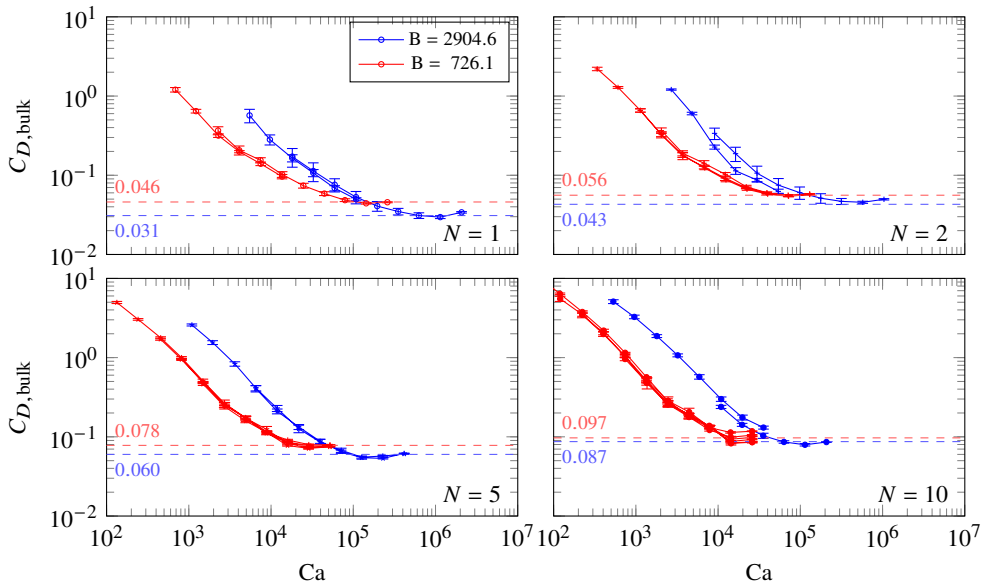


Figure 8: The effect of the buoyancy parameter  $B$  on  $C_{D,bulk}$  between Mimic 2 and Mimic 4 of the same aspect ratio  $l/b$  with different numbers of blades per bunch ( $N$ ). The dashed horizontal lines denotes  $C_{D,bulk}$  in the flutter regime.

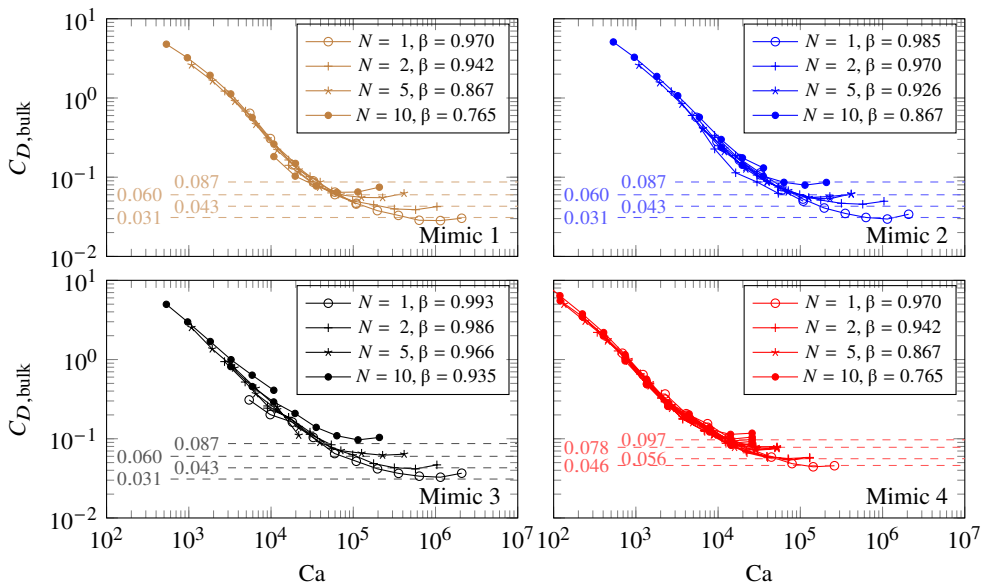


Figure 9: The effect of the mass ratio  $\beta$  on  $C_{D,bulk}$  for Mimics 1–4.  $\beta$  is computed with  $C_M = 1.0$ . The dashed horizontal lines denotes  $C_{D,bulk}$  in the flutter regime. For  $N = 10$ , we use the average  $C_{D,bulk} = 0.087$  from Mimic 1–3, see figure 7. For clarity, the error bars are not plotted.

---

Term	$C_{D,\text{bulk}}$ in static regime	System stability	$C_{D,\text{bulk}}$ in flutter regime
$\beta$	none	stabilizing	negatively correlated
B	positively correlated	stabilizing	depends on $\beta$ as well
$l/b$	none	none	none
$\lambda^*$	none	stabilizing	negatively correlated

---

Table 3: Effects of the non-dimensional parameters on  $C_{D,\text{bulk}}$  and the system stability.  
 \* The effects of  $\lambda$  are discussed in § 5.3.

and the system stability are summarized in table 3. These effects are consistent with the general trend shown in figure 6. In the static regime,  $C_{D,\text{bulk}}$  decreases monotonically until flutter occurs, after which it transitions to an almost constant value. For example,  $\beta$  has no effect on  $C_{D,\text{bulk}}$  in the static regime but plays a stabilizing role. As a result, a larger  $\beta$  will delay the onset of flutter, which in turn leads to a lower  $C_{D,\text{bulk}}$  in the flutter regime. The effects of B are more complicated. B and  $C_{D,\text{bulk}}$  are positively correlated in the static regime and meanwhile positive B stabilizes the system and delays the flutter. As a result, it is difficult to predict how  $C_{D,\text{bulk}}$  in the flutter regime will change with variations in B.

We want to emphasize that in the analysis, we have assumed a constant  $C_D = 1.95$  and  $C_D$  is included in the definition of Ca. An alternative definition of Ca without  $C_D$ , expressed as

$$\text{Ca} = \frac{1}{2} \frac{\rho b U^2 l^3}{EI}, \quad (4.2)$$

is also widely used (Gosselin *et al.* 2010; Jacobsen *et al.* 2019; Vettori *et al.* 2024). Using this alternative definition, the previous qualitative conclusions still hold. However, the curves plotted in logarithmic scales would be shifted a certain distance to the left.

## 5. Drag reduction

A flexible blade may experience less drag than a rigid blade of the same geometry, a phenomenon known as the drag reduction. In the theoretical analysis, it is preferable to quantify the extent of drag reduction rather than focusing on  $C_{D,\text{bulk}}$  with given  $C_D$  and  $C_M$ . In this section, we first introduce the reconfiguration number  $\mathcal{R}$  and the effective length  $l_e/l$ . We then present an analytical prediction of  $\mathcal{R}$  in the static regime, followed by a numerical prediction of  $\mathcal{R}$  in both the static and flutter regimes.

### 5.1. Reconfiguration number and effective length

Drag reduction can be quantified by using the reconfiguration number (Gosselin *et al.* 2010) or the effective length (Luhar & Nepf 2011). The reconfiguration number  $\mathcal{R}$  is defined as the ratio of the drag force on the deflected structure to that on a rigid counterpart of the same initial geometry. The effective blade length  $l_e$  is defined as the length of a rigid, vertical blade that would generate the same horizontal drag as the flexible blade of total length  $l$ . These two definitions are essentially equivalent, as expressed by:

$$\mathcal{R} = \frac{l_e}{l} = \frac{F}{F_{\text{rigid}}} = \frac{F}{1/2\rho C_D b l U^2}, \quad (5.1)$$

where  $U$  is the ambient horizontal velocity,  $F$  is the total horizontal drag on the deflected blade, and  $F_{\text{rigid}} = 1/2\rho C_D b l U^2$  is the total horizontal drag on the rigid, upright blade of the same dimensions. There are multiple ways to express  $F$ , consequently, leading to different approaches for calculating  $\mathcal{R}$  or  $l_e/l$ , existing in the literature.

In the static regime, following Luhar & Nepf (2011), the total drag force can be expressed as

$$F = \int_0^l \frac{1}{2} \rho C_D b (U \cos \theta)^2 \cos \theta \, ds, \quad (5.2)$$

where  $U \cos \theta$  is the local normal velocity accounting for the streamlined shape of the blade, and the final  $\cos \theta$  term in the integrand accounts for the horizontal component of the drag force or the reduced frontal area. In dimensionless form, using  $\tilde{s} = s/l$  as in § 3.1, the effective length is given by

$$\frac{l_e}{l} = \int_0^1 \cos^3 \theta \, d\tilde{s}, \quad (5.3)$$

which can also be used to calculate  $\mathcal{R}$  in the static regime, as in Gosselin *et al.* (2010). We denote this definition as  $\mathcal{R}^{\text{ana,g}}$ , where the superscript <sup>g</sup> stands for the *global* integral form over the interval  $0 \leq \tilde{s} \leq 1$ . It is worth noting that the concept of effective length has been more extensively used in the context of oscillatory flows in later studies (Luhar & Nepf 2016; Luhar *et al.* 2017; Lei & Nepf 2019a).

$F$  is also equal to the internal shear force at the base, i.e.,

$$F = Q(s=0) = -EI \left. \frac{\partial \kappa}{\partial s} \right|_{s=0}. \quad (5.4)$$

Inserting (5.4) into (5.1) gives  $\mathcal{R} = -\partial \tilde{\kappa} / \partial \tilde{s} (\tilde{s}=0) / \text{Ca}$ , as detailed in Leclercq *et al.* (2018). This definition is denoted as  $\mathcal{R}^{\text{ana,l}}$ , where the superscript <sup>l</sup> represents the *local* horizontal force balance at  $\tilde{s}=0$ .

In the post-critical regime, where flutter occurs, equations (5.2) and (5.3) are no longer applicable due to the blade's dynamic motion contributing to additional horizontal forces. In the experiments, it is more practical to use the measured horizontal force as  $F$  in (5.1), and the corresponding reconfiguration number is denoted as  $\mathcal{R}^{\text{exp}}$ . Theoretically,  $F$  is equal to the horizontal component of the total external force, which can be easily extracted in numerical models. In the numerical approach, we record  $F$  using this method. We denote the resulting reconfiguration number as  $\mathcal{R}^{\text{num}}$ . For the remainder of this study, we will use  $\mathcal{R}$  instead of  $l_e/l$  to represent drag reduction without loss of generality.

## 5.2. Analytical prediction

For velocities lower than the critical where fluttering occurs, the blade will reach a static equilibrium position. Removing all unsteady terms from (3.8) gives

$$\frac{\partial^2 \tilde{\kappa}}{\partial \tilde{s}^2} + \frac{1}{2} \tilde{\kappa}^3 + \beta \tilde{\kappa} \left( \tilde{U}_\tau^2 - \frac{1}{2} \tilde{U}_n^2 \right) + \beta \lambda |\tilde{U}_n| \tilde{U}_n + \text{B} \left( \tilde{\kappa} \int_1^{\tilde{s}} \cos \theta \, d\tilde{s} + \sin \theta \right) = 0 \quad (5.5)$$

Note that in static regime we have

$$\tilde{U}_n \mathbf{n} + \tilde{U}_\tau \boldsymbol{\tau} = -\frac{\mathbf{u}}{\sqrt{\beta}} \mathbf{e}_x = -\sqrt{\frac{\text{Ca}}{\beta \lambda}} \mathbf{e}_x, \quad (5.6)$$

which leads to

$$\tilde{U}_n = -\sqrt{\frac{\text{Ca}}{\beta \lambda}} \mathbf{e}_x \cdot \mathbf{n} = -\sqrt{\frac{\text{Ca}}{\beta \lambda}} \cos \theta, \quad \tilde{U}_\tau = -\sqrt{\frac{\text{Ca}}{\beta \lambda}} \mathbf{e}_x \cdot \boldsymbol{\tau} = -\sqrt{\frac{\text{Ca}}{\beta \lambda}} \sin \theta. \quad (5.7)$$

Inserting the expressions above and  $\tilde{\kappa} = \partial\theta/\partial\tilde{s}$  into (5.5) yields the static equation

$$\underbrace{\frac{\partial^3\theta}{\partial\tilde{s}^3} + \frac{1}{2}\left(\frac{\partial\theta}{\partial\tilde{s}}\right)^3}_{\text{bending stiffness}} + \underbrace{\frac{\text{Ca}}{\lambda}\frac{\partial\theta}{\partial\tilde{s}}\left(\sin^2\theta - \frac{1}{2}\cos^2\theta\right)}_{\text{reactive force}} - \underbrace{\left(\text{Ca}\cos^2\theta\right)}_{\text{drag}} + \underbrace{\text{B}\left(\frac{\partial\theta}{\partial\tilde{s}}\int_1^s\cos\theta d\tilde{s} + \sin\tilde{\theta}\right)}_{\text{buoyancy}} = 0, \quad (5.8)$$

with boundary conditions  $\theta = 0$  at  $\tilde{s} = 0$  and  $\partial\theta/\partial\tilde{s} = \partial^2\theta/\partial\tilde{s}^2 = 0$  at  $\tilde{s} = 1$ .

In the expression for bending stiffness, the second term arises from eliminating the tension using the inextensibility condition. If we neglect this term, along with the reactive force term, (5.8) simplifies to

$$\frac{\partial^3\theta}{\partial\tilde{s}^3} - \text{Ca}\cos^2\theta + \text{B}\left(\frac{\partial\theta}{\partial\tilde{s}}\int_1^s\cos\theta d\tilde{s} + \sin\theta\right) = 0, \quad (5.9)$$

which describes the force balance between bending stiffness, drag, and buoyancy. Luhar & Nepf (2011) derived an integral form of (5.9) by applying the force balance in the normal direction on an arbitrary arc extending from the blade tip.

If  $\text{B} = 0$ , (5.9) simplifies further to the form used by Gosselin *et al.* (2010)

$$\frac{\partial^3\theta}{\partial\tilde{s}^3} - \text{Ca}\cos^2\theta = 0, \quad (5.10)$$

which represents a force balance between bending stiffness and drag.

Luhar & Nepf (2011) first solved the integral form of (5.9) (their equation (6)) to obtain  $\theta(\tilde{s})$  and then used (5.3) to calculate the effective length. Similarly, Gosselin *et al.* (2010) solved (5.10) and subsequently obtained  $\mathcal{R}^{\text{ana,g}}$  (their equations (5.15) and (5.16)). In both cases, the second term in the bending stiffness,  $1/2(\partial\theta/\partial\tilde{s})^3$ , is omitted. As a result, equations (5.9) and (5.10) essentially model a small-amplitude Euler-Bernoulli beam without considering tension effects. This omission leads to an inconsistency between the definitions of  $\mathcal{R}^{\text{ana,g}}$  and  $\mathcal{R}^{\text{ana,l}}$ , i.e.,

$$\int_0^1 \cos^3\theta d\tilde{s} = \mathcal{R}^{\text{ana,g}} \neq \mathcal{R}^{\text{ana,l}} = -\left.\frac{\partial\tilde{\kappa}}{\partial\tilde{s}}\right|_{\tilde{s}=0}. \quad (5.11)$$

Therefore, caution is needed when comparing  $\mathcal{R}^{\text{ana,g}}$  derived from equations (5.9) and (5.10) with experimental data. In the experiments, the forces at the base of the blade instead of the total forces on the blade are measured. Additionally, tension effects are always present in reality. Consequently, when comparing analytical prediction with experimental result,  $\mathcal{R}^{\text{ana,l}}$  would be a more appropriate choice than  $\mathcal{R}^{\text{ana,g}}$ .

To solve (5.8), we follow the approach of Leclercq *et al.* (2018) and Leclercq & de Langre (2018). We first discretize the blade using the Gauss-Lobatto distribution  $s_k = 1/2[1 - \cos((k-1)/(N-1)\pi)]$  along with the boundary conditions. The derivatives and integrals are then computed using Chebyshev collocation and the Clenshaw-Curtis quadrature formulae, respectively. The analytical predictions of  $\mathcal{R}$  are plotted together with the experimental data in figure 10.

Using the analytical model, we can examine the effect of  $\lambda$ . With the same  $\text{B}$ , all curves for different  $\lambda$  coincide at small  $\text{Ca}$  until the curve for smaller  $\lambda$  changes its rate of decrease and starts to deviate. As  $\lambda$  increases, the curve approaches the solution without the reactive force term in (5.8) by letting  $\lambda \rightarrow \infty$ .

When comparing the analytical predictions with the experimental data in the static regime, we find that  $\lambda$  plays a significant role. Specifically, large  $\lambda$  provides better agreement of  $\mathcal{R}$  for both  $\text{B}$  values before flutter occurs. As discussed in § 3.1, the drag reduction should be



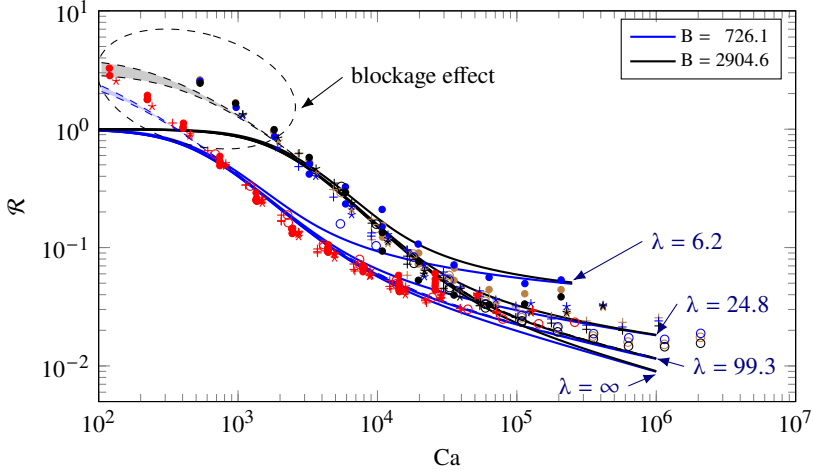


Figure 10: The analytical predictions of  $\mathcal{R}$  with different  $\lambda$  (lines) and the experimental data (markers). The dashed lines are analytical predictions of  $\mathcal{R}$  accounting for the blockage effect. The shaded areas between the dashed lines are bounded by  $\delta/b = 0$  and  $0.05$ . Mimic 1–4 are respectively represented in brown, blue, black, and red. The number of blade per bunch  $N$  is represented by different markers: circle  $\circ$ ,  $N = 1$ ; plus  $+$ ,  $N = 2$ ; five-pointed star  $\star$ ,  $N = 5$ ; dot  $\bullet$ ,  $N = 10$ .

a function of the four non-dimensional parameters, i.e.,  $\mathcal{R} = \mathcal{R}(Ca, B, \beta, \lambda)$ . In the static regime, all terms involving  $\beta$  are gone and there is  $\mathcal{R} = \mathcal{R}(Ca, B, \lambda)$ . If we look at the experimental data with same  $B$ ,  $\mathcal{R}$  is independent on  $\lambda$  if constant  $C_D$  and  $C_M$  are assumed as shown in figure 7 since  $\lambda = (2/\pi)(C_D/C_M)(l/b)$ . On the other hand, the analytical results indicate that  $\mathcal{R}$  strongly depends on  $\lambda$ . There are two possible explanations for this observation: 1)  $\lambda$  has minimal impact on  $C_{D, \text{bulk}}$  or  $R$ . The reactive force term, which involves  $\lambda$ , should be excluded from (5.8). Since this term arises from the last two terms in (3.4) (see § 5.3.2), the reactive force model should be simplified to include only the first term. 2) The reactive force term should remain in (5.8) and (3.4) is the proper hydrodynamic load model. In the scenario of side-by-side blades,  $l/b$  may alter  $C_D$  and  $C_M$ , leading to the same  $\lambda$ . Consequently, the effect of the aspect ratio appears to be minor, as discussed in § 4.2. This issue is further investigated, and the conclusion is drawn in § 5.3, where the numerical model is employed to study the system stability and drag reduction in the flutter regime and to examine the reactive force model term by term.

$\mathcal{R}^{\text{ana},1}$  always starts from 1 at  $Ca = 0$ , and remains almost constant before beginning a monotonic decrease. If  $B = 0$ , solving (5.10) shows that  $\mathcal{R}^{\text{ana},1}$  starts to decrease around  $Ca = 1$ . Since  $Ca$  represents the ratio of the drag to the bending stiffness,  $Ca < 1$  indicates the blade is stiff while  $Ca > 1$  denote flexibility. In other words, when  $Ca \ll 1$ , the deflection is negligibly small and the blade remains almost vertically suspended. When  $Ca \gg 1$ , the blade is significantly deflected by the flow.

In scenarios where  $B > 0$  and the structures under consideration are heavier than water, we can expect that  $\mathcal{R}$  will begin to decrease from 1 at a higher  $Ca$  compared to  $B = 0$ . Dividing (5.9) with  $B$  provides

$$\frac{1}{B} \frac{\partial^3 \theta}{\partial \bar{s}^3} + \frac{Ca}{B} \cos^2 \theta + \left( \frac{\partial \theta}{\partial \bar{s}} \int_1^s \cos \theta d\bar{s} + \sin \theta \right) = 0, \quad (5.12)$$

where  $Ca/B$  represents the ratio of drag and buoyancy. Physically, the blade undergoes significant deflection when  $Ca \gg 1$  as previously discussed and  $Ca/B \gg 1$ . Otherwise, the

drag force is insufficient to overcome the restoring forces, including both the bending stiffness and the effective weight. As a result,  $\mathcal{R}$  is approximately 1 when  $\text{Ca}/B < O(1)$  and starts to decrease at  $\text{Ca}/B \approx O(1)$ . This conclusion is consistent with the analytical predictions but not the experimental data due to the blockage effect.

The analytical model discussed earlier considers an individual blade in an infinite fluid domain. However, in the experiments, the side-by-side blades will block the flow significantly at  $\text{Ca}/B < 1$  when the deflection of blades is small, leading to an overestimation of  $C_{D,\text{bulk}}$  as shown in figure 6. We treat the side-by-side blades as a blade with "holes" or "gaps" on it. By considering the physical problem of a flexible rectangular blades in a limited fluid domain as illustrated in figure 4b, we introduce another three quantities, the submergence  $d_1$  the blade, the distance  $d_2 - h_{\text{proj}}$  from the blade tip to the tank bottom, and the gaps  $\delta$ . Instead of introducing another three non-dimensional parameters, we follow the approach in studies of perforated plates to include the three quantities in the perforation ratio since the local effective speed is the most important quantity. There are two factors contributing to the perforation (or inversely the blockage) as shown in figure 4b, the gaps above and below the blades as well as the gaps between the blades due to rotations or motion out of phase. To account for the blockage effect, we define the solidity ratio

$$\text{Sn} = \frac{h_{\text{proj}}}{h} \left( 1 - \frac{\delta}{b} \right), \quad (5.13)$$

where  $h_{\text{proj}}$  is the project height of the blades in the  $yz$ -plane,  $h = 0.61$  m is water depth, and  $\delta$  is the average gap between two bunches of blades, as illustrated in figure 4b. The gaps between the acrylic plates and the side walls are relatively small compared to the tank width and will be neglected.

For example, when  $U = 0$  and the blades are hanging vertically downward in the water,  $\text{Sn} \approx 5/6$ . As  $U$  increases, the blades become more aligned with the horizontal direction, causing  $\text{Sn}$  to decrease. The local effective velocity at the blades (or over the blade span in  $x$ -direction) can be approximated by  $U^{\text{local}} = U/(1 - \text{Sn})$ , where the factor  $1/(1 - \text{Sn})$  accounts for the local speed-up of the flow as it passes around the blades, due to mass conservation.

The local  $\text{Ca}^{\text{local}}$  can then be expressed as  $\text{Ca}^{\text{local}} = \text{Ca}/(1 - \text{Sn})^2$  from  $\text{Ca}^{\text{local}}/\text{Ca} = (U^{\text{local}}/U)^2$ . Using this relation, we adjust the analytical solution (represented by solid curves in the figure 10) as follows:

- (i) For a given  $\text{Ca}$ , solve (5.8) to obtain  $h_{\text{proj}} = \int_0^1 \cos \theta d\tilde{s}$  and  $\mathcal{R}^{\text{ana},1}$ , and compute  $\text{Sn}$  using (5.13).
- (ii) Update  $\text{Ca}^{\text{local}} = \text{Ca}/(1 - \text{Sn})^2$ .
- (iii) With the updated  $\text{Ca}^{\text{local}}$ , solve (5.8) again to obtain updated  $h_{\text{proj}}$  and  $\mathcal{R}^{\text{ana},1}$ , and compute  $\text{Sn}$ .
- (iv) Repeat Steps (ii) and (iii) until  $\mathcal{R}^{\text{ana},1}$  converges.
- (v) Calculate the corrected  $\mathcal{R}^{\text{CWT}} = \mathcal{R}(\text{Ca}^{\text{local}})\text{Ca}^{\text{local}}/\text{Ca}$ .

Through this iterative approach, we determine  $\text{Ca}$  using the known upstream velocity and compute the corresponding  $\mathcal{R}$  at this velocity, including the effects of blockage. This allows us to compare the analytical solution with the experimental data. As shown in figure 10, the blockage effect is significant only at low  $\text{Ca}$ . At high  $\text{Ca}$ , the blades align with the flow direction, and the solidity ratio approaches zero. When accounting for the blockage effect, the analytical predictions at small  $\text{Ca}$  generally align with the experimental data, although they are slightly lower.

In conclusion, the analytical model is capable of predicting the drag reduction in the static

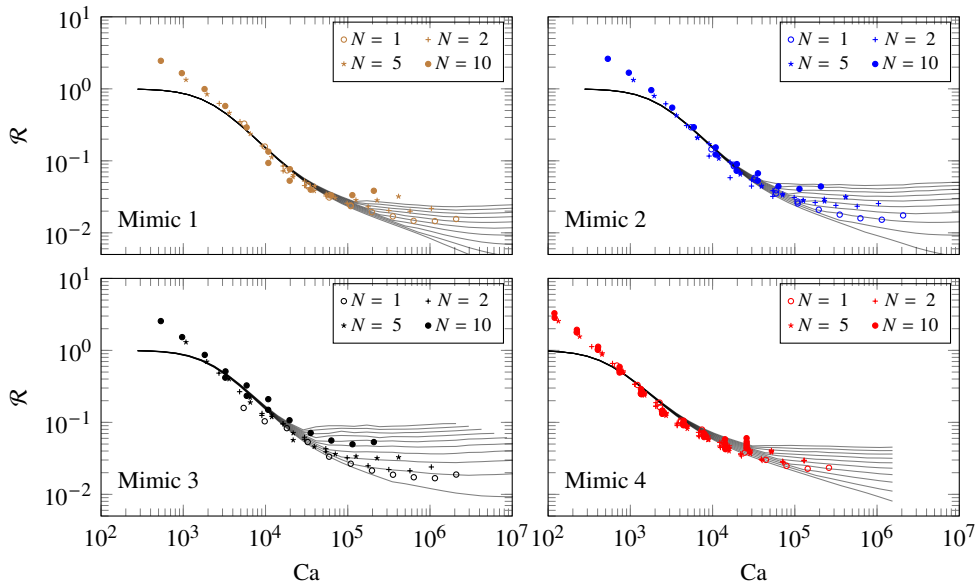


Figure 11: The numerical predictions of  $\mathcal{R}$  with different  $\lambda$  (lines) and the experimental data (markers). The  $\lambda$  values for some lines are annotated in figure 12.

regime. At small  $Ca$ , if the blockage effect is significant, the estimate should be adjusted based on the solidity ratio.

### 5.3. Numerical prediction

We utilize the numerical model developed by Wei *et al.* (2024) to investigate drag reduction in both the static and flutter regimes. In this section, utilizing the numerical model, we examine the impact of the slenderness parameter and delve into the hydrodynamic load model, with a particular focus on the reactive force.

#### 5.3.1. Effect of the slenderness parameter

We have determined from model tests that  $l/b$  has minimal influence on  $C_{D,\text{bulk}}$  in both the static and flutter regimes, as discussed in § 4.2. On the other hand,  $\lambda$  plays a significant role from the analytical solutions in the static regime as outlined in § 5.2. We now proceed to investigate the effect of  $\lambda$  in the flutter regime.

$\mathcal{R}^{\text{num}}$  is compared to  $\mathcal{R}^{\text{exp}}$  in figure 11. An enlarged view of only the flutter regime is provided in figure 12. Snapshots from our numerical model illustrating the transition from the static reconfiguration to flutter of Mimic 2 with  $C_M = 1.0$  and  $N = 1$  are provided in figure 13. We fix  $C_D = 1.95$  and adjust  $C_M$  from 0.1 up to 1.0 to change  $\lambda$  for each blade mimic. In the static regime, the numerical predictions closely match the experimental data for all  $\lambda$ . However,  $\lambda$  plays a significant role in determining the critical  $Ca$  and  $\mathcal{R}$  in the flutter regime. A larger  $\lambda$  delays the onset of flutter and results in a smaller  $\mathcal{R}$  within the flutter regime. If the case of  $\lambda \rightarrow \infty$ , no flutter occurs. To replicate the flutter observed in the experiments,  $\lambda$  must be retained, and the terms involving  $\lambda$ , i.e., the last two terms in (3.4) must also be included in the hydrodynamic load model. If so, why  $l/b \propto \lambda$  has minimal effect on  $C_{D,\text{bulk}}$  or  $\mathcal{R}$ ?

With specific values of  $C_M$  and  $\lambda$ , the numerical model accurately predicts both the critical  $Ca$  and  $\mathcal{R}$  in the flutter regime. For Mimic 1–3, which have different  $l/b$ , similar values of  $\lambda$  are required to align  $\mathcal{R}^{\text{num}}$  with  $\mathcal{R}^{\text{exp}}$ . From the definition of  $\lambda$ , this implies that  $C_D/C_M$

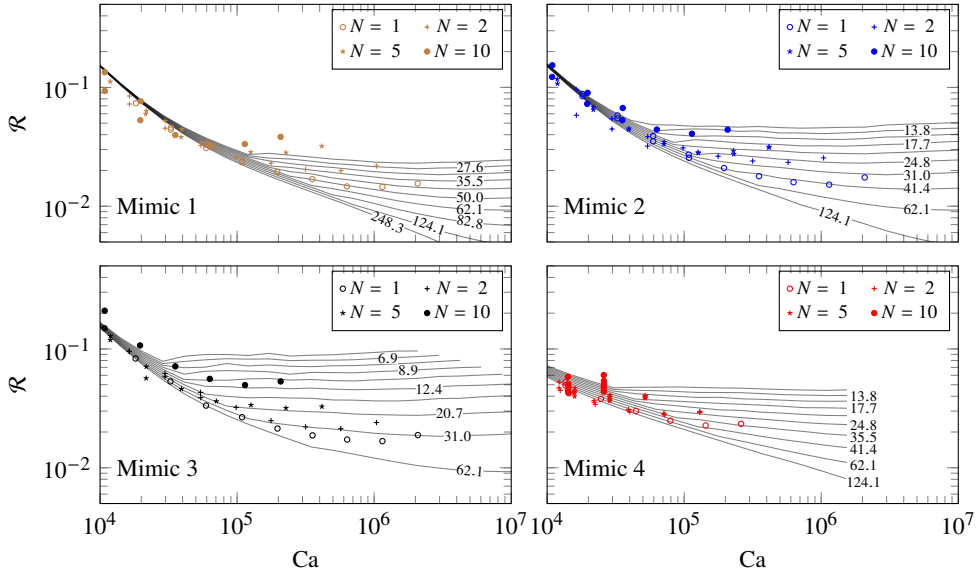


Figure 12: The numerical predictions of  $\mathcal{R}$  with different  $\lambda$  (lines) and the experimental data (markers) in the flutter regime. Some  $\lambda$  values are annotated on or beside the lines.

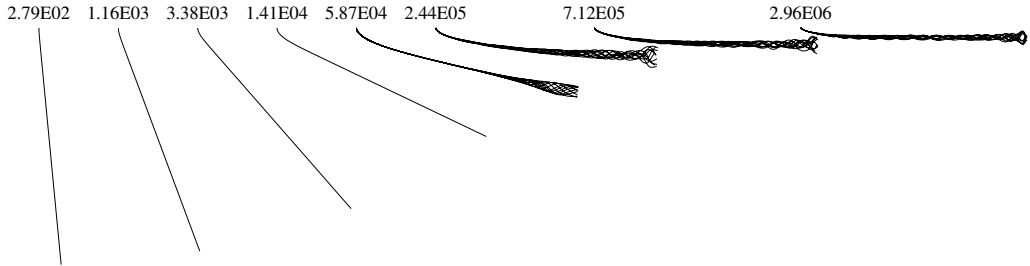


Figure 13: Blade reconfiguration transitioning from the static to the flutter regime of Mimic 2 with  $C_M = 1.0$  in the numerical model. The corresponding  $Ca$  is indicated above each image.

must be inversely proportional to  $l/b$  to maintain the same  $\lambda$ . Based on the assumption that  $C_D$  is fixed, it follows that  $C_M$  is inversely proportional to  $l/b$ . Given the numerical model adequately represents the physics, we conclude that for side-by-side blades, the cross-flow hydrodynamic coefficients  $C_D$  and  $C_M$  are influenced by the blade's aspect ratio  $l/b$  such that  $\lambda = 2/\pi(C_D/C_M)(l/b)$  remains nearly constant.

From these results, we argue that our numerical model has sufficient physics incorporated to capture the onset of flutter, and even to predict the (nearly  $Ca$ -independent)  $\mathcal{R}$  within the flutter regime, as evidenced by the curves with varying  $\lambda$ . A remaining question is, though, the value of  $C_M$ , which is used to vary  $\lambda$ . The  $C_M$  coefficient is at present only chosen heuristically. Obtaining physically-based values for  $C_M$  would advance our model's accuracy significantly. We see this as a possibility, where the proximity to the neighbor specimen is considered as a main element to include. One can perform forced motions of a single blade with other neighbor blades, in relevant configurations relative to each other, in a dedicated numerical study. However, we leave this as a future study.

### 5.3.2. Discussion on the reactive force model

Using the numerical model, we can investigate the effect of each term in the reactive force model, i.e., (3.4), by selectively disabling them in our simulations. By tracing the origin of the terms in (3.8), we identify how each term in (3.4) contributes to (3.8) and to the static terms in (5.8):

$$\begin{aligned} \mathbf{q}_{am,1} &\sim -\frac{\partial(U_n \mathbf{n})}{\partial t} \rightarrow \frac{\partial^2 \tilde{\mathbf{r}}}{\partial \tilde{t}^2} \cdot \mathbf{n} - \tilde{U}_\tau \frac{\partial \theta}{\partial \tilde{t}} \xrightarrow{\text{static}} 0, \\ \mathbf{q}_{am,2} &\sim \frac{\partial(U_\tau U_n \mathbf{n})}{\partial s} \rightarrow -\tilde{U}_\tau \frac{\partial \theta}{\partial \tilde{t}} + \tilde{\kappa} \tilde{U}_\tau^2 \xrightarrow{\text{static}} \frac{\text{Ca}}{\lambda} \frac{\partial \theta}{\partial \tilde{s}} \sin^2 \theta, \\ \mathbf{q}_{am,3} &\sim -\frac{1}{2} \frac{\partial(U_n^2 \boldsymbol{\tau})}{\partial s} \rightarrow -\frac{1}{2} \tilde{\kappa} \tilde{U}_n^2 \xrightarrow{\text{static}} -\frac{1}{2} \frac{\text{Ca}}{\lambda} \frac{\partial \theta}{\partial \tilde{s}} \cos^2 \theta. \end{aligned}$$

In the traditional Morison's equation, only  $\mathbf{q}_{am,1}$  is included, and we choose to retain this term. There are two terms in  $\mathbf{q}_{am,2}$ , which are further denoted by

$$\mathbf{q}_{am,2,1} = -\tilde{U}_\tau \frac{\partial \theta}{\partial \tilde{t}}, \quad \mathbf{q}_{am,2,2} = \tilde{\kappa} \tilde{U}_\tau^2. \quad (5.14)$$

By testing eight different combinations of including or excluding the terms  $\mathbf{q}_{am,2,1}$ ,  $\mathbf{q}_{am,2,2}$ , and  $\mathbf{q}_{am,3}$  in the hydrodynamic load model, the corresponding  $\mathcal{R}^{\text{num}}$  are plotted in figure 14. Upon analyzing each term, we find the following effects.

$\mathbf{q}_{am,2,2}$  has a destabilizing effect. When this term is included (e.g., Codes 111 and 110), flutter occurs. Conversely, when this term is excluded (e.g., Codes 101 and 100), no flutter is observed. This indicates that  $\mathbf{q}_{am,2,2}$  contributes to the system instability.

$\mathbf{q}_{am,2,1}$  has a stabilizing effect. Including  $\mathbf{q}_{am,2,1}$  alongside  $\mathbf{q}_{am,2,2}$  (e.g., Codes 111 and 110) allows flutter to occur without causing the simulation to crash. However, excluding  $\mathbf{q}_{am,2,1}$  while including  $\mathbf{q}_{am,2,2}$  (e.g., Codes 011 and 010) leads to simulation crashes. There is one term the same as  $\mathbf{q}_{am,2,1}$  in  $\mathbf{q}_{am,1}$ . Later we can see that excluding  $\mathbf{q}_{am,2,1}$  effectively corresponds to reducing  $\beta$  to one quarter of its original value while maintaining the original load model. This adjustment significantly lowers the critical Ca, as illustrated in Figure 3 of Leclercq *et al.* (2018). In scenarios where  $\mathbf{q}_{am,2,2}$  is excluded and no flutter occurs, the transient term  $\mathbf{q}_{am,2,1}$  diminishes and has no effect on  $\mathcal{R}$  due to the static reconfiguration at all Ca (e.g., comparison between Codes 000 and 100, Codes 001 and 101).

$\mathbf{q}_{am,3}$ , included or not, will not prevent flutter or alter its onset, but modifies  $\mathcal{R}$  (e.g., comparison between Codes 111 and 110, Codes 000 and 001).

In conclusion, all terms in the reactive force model matter and should be included. The traditional Morison's equation, in which only  $\mathbf{q}_{am,1}$  is included alongside with the drag, is insufficient to trigger flutter or predict the drag reduction in application of highly compliant structures. At low Ca, when the blades are perpendicular to the inflow, there is mainly cross-flow separation and wake formation along the length of the blades. At high Ca, the structure aligns with the flow and the hydrodynamic load models, e.g., equations (3.3) and (3.4), are more appropriate.

Leclercq *et al.* (2018) concluded that the relative magnitude of the reactive fluid force and the structural stiffness determines the onset of flutter instead of the magnitude of the resistive drag, which can be represented by the reduced velocity

$$u^2 = \frac{\text{Ca}}{\lambda} = \frac{m_a U^2 l}{EI}. \quad (5.15)$$

The reduced velocity is commonly used when discussing features of the flutter instability. If we plot the numerical predictions of  $\mathcal{R}$  with respect to  $u$  instead of Ca, the regime transition

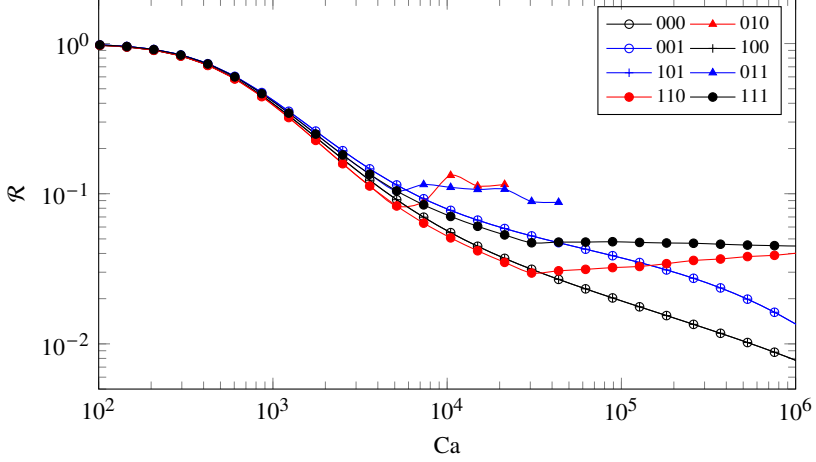


Figure 14: The numerical prediction of  $\mathcal{R}$  for Mimic 4 with different combinations of the three terms in the reactive force model. The three codes represent  $\mathbf{q}_{am,2,1}$ ,  $\mathbf{q}_{am,2,2}$ , and  $\mathbf{q}_{am,3}$ , respectively. 1 means the corresponding term is included, and 0 means that term is excluded.

points will be aligned at approximately the same  $u$ , or the critical  $u$  depends little on  $\lambda$ , which again is consistent with Leclercq *et al.* (2018). Meanwhile,  $\mathcal{R}$  in the static regime will not follow the same curve. Since this paper focuses on the drag reduction,  $Ca$  would be more appropriate choice than  $u$ .

The classic non-dimensional small-amplitude flutter equation for an undamped beam in axial flow (Paidoussis 1998) can be written as

$$\frac{\partial^2 \tilde{\eta}}{\partial \tilde{t}^2} + 2u\sqrt{\beta} \frac{\partial^2 \tilde{\eta}}{\partial \tilde{t} \partial \tilde{s}} + u^2 \frac{\partial^2 \tilde{\eta}}{\partial \tilde{s}^2} + \frac{\partial^4 \tilde{\eta}}{\partial \tilde{s}^4} = 0, \quad (5.16)$$

with boundary conditions  $\tilde{\eta} = \partial \tilde{\eta} / \partial \tilde{s} = 0$  at  $\tilde{s} = 0$  and  $\partial^2 \tilde{\eta} / \partial \tilde{s}^2 = \partial^3 \tilde{\eta} / \partial \tilde{s}^3 = 0$  at  $\tilde{s} = 1$ , where  $\tilde{\eta}(\tilde{s}, \tilde{t})$  is the normalized lateral displacement, and the other symbols have the same definition as in this paper. By comparing the terms in the reactive force with the terms in (5.16), we find the following relations:

$$\begin{aligned} \mathbf{q}_{am,1} &\sim \frac{\partial^2 \tilde{\mathbf{r}}}{\partial \tilde{t}^2} \cdot \mathbf{n} - \tilde{U}_\tau \frac{\partial \theta}{\partial \tilde{t}} && \sim \frac{\partial^2 \tilde{\eta}}{\partial \tilde{t}^2} + u\sqrt{\beta} \frac{\partial}{\partial \tilde{t}} \left( \frac{\partial \tilde{\eta}}{\partial \tilde{s}} \right), \\ \mathbf{q}_{am,2,1} &\sim -\tilde{U}_\tau \frac{\partial \theta}{\partial \tilde{t}} && \sim u\sqrt{\beta} \frac{\partial^2 \tilde{\eta}}{\partial \tilde{t} \partial \tilde{s}} = u\sqrt{\beta} \frac{\partial}{\partial \tilde{t}} \left( \frac{\partial \tilde{\eta}}{\partial \tilde{s}} \right), \\ \mathbf{q}_{am,2,2} &\sim \tilde{\kappa} \tilde{U}_\tau^2 = \tilde{U}_\tau^2 \frac{\partial \theta}{\partial \tilde{s}} \xrightarrow{\text{static}} u^2 \frac{\partial \theta}{\partial \tilde{s}} \sin^2 \theta \xrightarrow{\theta \rightarrow \pi/2} u^2 \frac{\partial \theta}{\partial \tilde{s}} \sim u^2 \frac{\partial^2 \tilde{\eta}}{\partial \tilde{s}^2} = u^2 \frac{\partial}{\partial \tilde{s}} \left( \frac{\partial \tilde{\eta}}{\partial \tilde{s}} \right), \\ \mathbf{q}_{am,3} &\sim -\frac{1}{2} \tilde{\kappa} \tilde{U}_n^2 \xrightarrow{\text{static}} -\frac{1}{2} \frac{Ca}{\lambda} \frac{\partial \theta}{\partial \tilde{s}} \cos^2 \theta \xrightarrow{\theta \rightarrow \pi/2} 0 \quad \sim 0. \end{aligned}$$

According to the small-amplitude motion assumption,  $\partial \tilde{\eta} / \partial \tilde{s} \simeq \tan \alpha \simeq \alpha$ , where  $\alpha = \pi/2 - \theta$ . In the appendix of Leclercq *et al.* (2018), it has been demonstrated that (5.16) cannot be used to predict the onset of flutter. This limitation arises from the presence of drag, which is caused by the distinct boundary conditions of an upright clamped blade. Since the stability theory of (5.16) has been well developed (Paidoussis 1998), we can still use it to qualitatively check the conclusions drawn previously on the different terms in the reactive force model regarding the system stability.

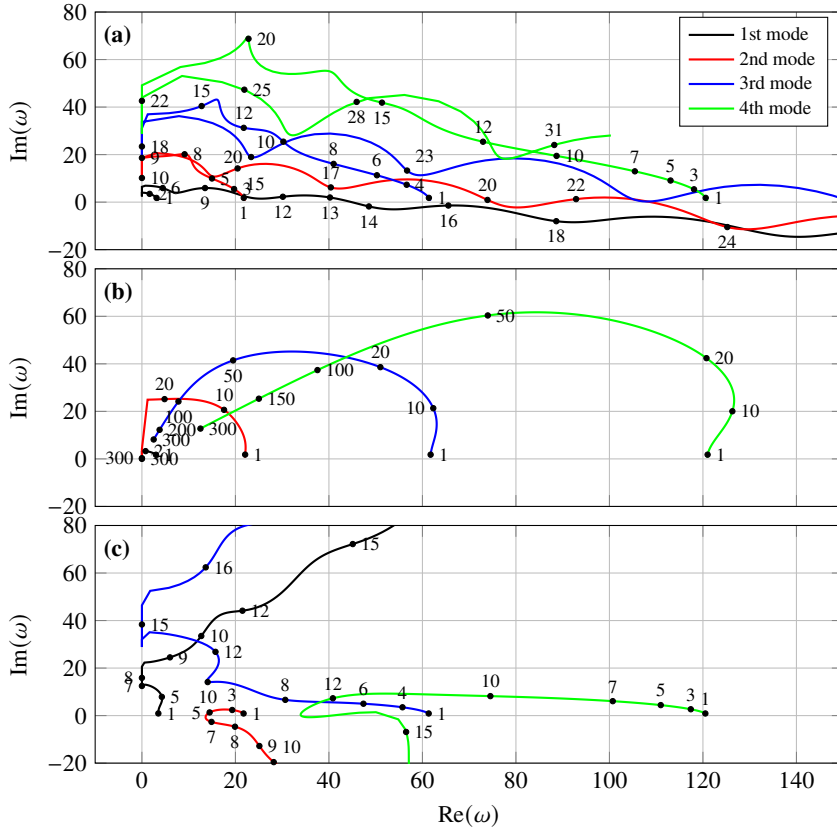


Figure 15: The dimensionless complex frequency of the four lowest modes of the system ( $\beta = 0.8$ ) as a function of the reduced velocity annotated along the curves. (a) All terms are included; (b) The third term in (5.16) is excluded; (c) The second term in (5.16) is reduced to its half.

We set  $\beta = 0.8$ , which fall within the range of our experiments (see table 2). Following the method of Paidoussis (1998), we apply the Galerkin method using the first twelve modes in the Galerkin expansion to solve (5.16). The dimensionless complex frequencies of the four lowest modes are plotted in figure 15. Although not shown, the remaining modes were also examined to determine the system stability. A negative imaginary part of the complex frequency, i.e.,  $\text{Im}(\omega)$  below zero in figure 15, means instability. When all terms are included, instability initiates in the first mode at  $u \approx 13.5$ . If the third term in (5.16), the counterpart of  $\mathbf{q}_{am,2,2}$ , is disabled, all modes remain stable regardless of the value of  $u$ . In this scenario, the first mode rapidly approaches the origin and diminishes. If the second term in (5.16) is reduced by half, effectively deactivating the counterpart of  $\mathbf{q}_{am,2,1}$ , the system loses its stability in the second mode first at  $u \approx 6$  instead of in the first mode. In fact, for (5.16), halving the second term is equivalent to reducing  $\beta$  to one quarter of its original value meanwhile solving the original (5.16). This is illustrated in figure 15c, which corresponds to Figure 3.30 of Paidoussis (1998) where  $\beta = 0.2$  was assumed.

Decreasing  $\beta$  significantly lowers the critical  $u$ , as shown in Figure 3.33 of Paidoussis (1998) for the linear stability of (5.16), and in Figure 2 of Leclercq *et al.* (2018) for scenarios involving drag, as studied in this paper. In conclusion, our findings are consistent with these previous studies regarding the effects of the different terms in the reactive force model.



## 6. Conclusion

This study presents a thorough and systematic investigation, utilizing both experimental and theoretical approaches, into the hydrodynamic drag loads on side-by-side clusters of flexible blades in a uniform current. A total of 176 combinations of blade properties (including dimensions and the number of overlapping layers in each bunch) and current speeds were tested. The experiments covered two distinct reconfiguration regimes: static and flutter. We examine four non-dimensional parameters, the Cauchy number, the buoyancy parameter, the mass ratio, and the slenderness parameter to assess their effects on the bulk drag coefficient for side-by-side blades and the onset of flutter. When excluding the blockage effect, the bulk drag coefficient remains constant at low Cauchy numbers less than the buoyancy parameter, decreases at moderate Cauchy numbers larger than the buoyancy parameter until flutter occurs, and then transitions to an approximately constant value in the flutter regime at high Cauchy numbers. In the static regime, the bulk drag coefficient is mainly positively correlated with the buoyancy parameter. The onset of flutter will be delayed to larger  $Ca$  by increasing the buoyancy parameter, the mass ratio, or the slenderness parameter. In the flutter regime, a larger mass ratio or slenderness parameter results in a lower bulk drag coefficient. Notably, the aspect ratio (length to width) is found to have negligible effect on the bulk drag coefficient or the onset of flutter for side-by-side blades.

An analytical model is developed based on the static governing equation of motion for an individual blade, incorporating the concepts of equivalent thickness and bending stiffness to represent a bunch of blades. This strategy proves efficient for modeling multiple overlapping blades. The analytical model accurately predicts drag reduction in the static regime. Furthermore, a numerical model using the same strategy of equivalent thickness and bending stiffness effectively predicts the onset of flutter and drag reduction in both regimes, given certain cross-flow hydrodynamic coefficients.

Through a review of the various terms in the reactive force model, we identify the term responsible for inducing instability, the term that stabilizes the system, and the term that purely modifies drag reduction. The similarity between the present model and the classic small-amplitude flutter equation for an undamped cantilever beam in axial flow further corroborates these conclusions. Our findings indicate that the traditional Morison's equation, which accounts only for the relative acceleration term in the reactive force, is insufficient to induce flutter.

The data set presented in this work is expected to be a valuable resource for engineering applications, aiding in the estimation of loads on side-by-side flexible blades. It also serves as a benchmark for theoretical models investigating hydrodynamic loads on such blade arrangements. Our findings on the reactive force support its use over Morison's equation in scenarios involving highly compliant blades in cross flow.

**Supplementary data.** The supplementary material available at <https://doi.org/10.11583/DTU.27180579.v1> includes 1) a Python script for solving the static governing equation (5.8), 2) a complete list of all test cases, 3) a lossless version of figure 2, 4) several animations of the numerical simulations, 5) several videos recorded during the experiments, and 6) a Python script for solving the small-amplitude flutter equation (5.16) for an undamped cantilever beam in axial flow.

**Acknowledgements.** Z. Wei acknowledges the support and assistance provided by the laboratory staff at NTNU.

**Funding.** Z. Wei and Y. Shao would like to acknowledge the financial support from Alliance Scholarships at Technical University of Denmark. T. Kristiansen and D. Kristiansen acknowledge partial support from the Research Council of Norway through SFI BLUES, grant number 309281.

**Declaration of interests.** The authors report no conflict of interest.

**Data availability statement.** The code used for numerical model is preserved at <https://doi.org/10.>

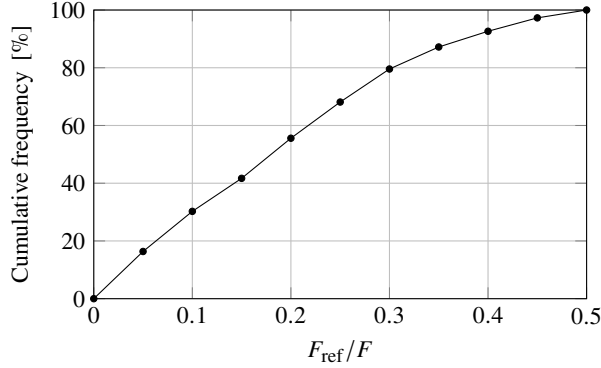


Figure 16: Contribution from the drag force on the frame  $F_{\text{ref}}$  to the total drag force  $F$ .

11583/DTU.24533098.v3, meanwhile available under the MIT License and developed openly at <https://gitlab.gbar.dtu.dk/floatingseaweedfarms/wavevegetationinteraction>.

## Appendix A. Uncertainty analysis

There are multiple sources contributing to the uncertainty of  $C_{D,\text{bulk}}$ . In our experiments, we measured the total forces acting on both the blades and the holding frame. To determine the forces on the blades alone, we subtracted the forces on the frame from the total measured forces. This calculation assumes there is no interaction between the blades and the struts or the acrylic plates—a factor introducing uncertainty that cannot be directly and accurately quantified. The proportion of the force on the frame  $F_{\text{ref}}$  to the total measured force  $F$  is examined, as shown in figure 16. In all test cases,  $F_{\text{ref}}$  contributed less than 50% of  $F$ . In nearly 60% of the test cases,  $F_{\text{ref}}$  contributed less than 20% of  $F$ . In most cases, the force acting on the blades was significantly greater than that on the frame. Although the uncertainty from subtracting the frame’s force cannot be precisely quantified, its effect on the bulk drag coefficient is minimal.

However, the uncertainty arising from the variability of the three repetitions of each test condition and from the errors in the material’s Young’s modulus are quantifiable. The standard errors of  $C_{D,\text{bulk}}$  and  $\text{Ca}$  are calculated as follows:

$$\delta C_{D,\text{bulk}} = \sqrt{\left(\delta F \frac{\partial C_{D,\text{bulk}}}{\partial F}\right)^2 + \left(\delta U \frac{\partial C_{D,\text{bulk}}}{\partial U}\right)^2}, \quad (\text{A } 1)$$

$$\delta \text{Ca} = \sqrt{\left(\delta U \frac{\partial \text{Ca}}{\partial U}\right)^2 + \left(\delta E \frac{\partial \text{Ca}}{\partial E}\right)^2}, \quad (\text{A } 2)$$

where the uncertainties in the horizontal force and velocity,  $\delta F$  and  $\delta U$  are given by:

$$\delta F = t_n \sqrt{\frac{1}{n(n-1)} \sum_{i=1}^n (F_i - \bar{F})^2}, \quad \delta U = t_n \sqrt{\frac{1}{n(n-1)} \sum_{i=1}^n (U_i - \bar{U})^2}, \quad n = 3, \quad (\text{A } 3)$$

and  $\bar{F}$  and  $\bar{U}$  are the means of the force and velocity measurements  $F_i$  and  $U_i$ , respectively. The factor  $t_n = 1.32$  in (A 3) is used due to the small sample size  $n = 3$ , ensuring 68.3% confidence intervals (Student 1908).

## REFERENCES

- BASKARAN, MRUDHULA, HUTIN, LOUIS & MULLENNERS, KAREN 2023 Reconfiguring it out: How flexible structures interact with fluid flows. *Physical Review Fluids* **8** (11), 110509.
- BOUKOR, MARYAM, CHOIMET, AUGUSTIN, LAURENDEAU, ÉRIC & GOSSELIN, FRÉDÉRIK P. 2024 Flutter limitation of drag reduction by elastic reconfiguration. *Physics of Fluids* **36** (2), 021915.
- BUCK, BELA HIERONYMUS & BUCHHOLZ, CORNELIA MARIA 2005 Response of offshore cultivated *Laminaria saccharina* to hydrodynamic forcing in the North Sea. *Aquaculture* **250** (3-4), 674–691.
- BUCKINGHAM, E. 1914 On Physically Similar Systems; Illustrations of the Use of Dimensional Equations. *Physical Review* **4** (4), 345–376.
- CAMPBELL, IONA, MACLEOD, ADRIAN, SAHLMANN, CHRISTIAN, NEVES, LUIZA, FUNDERUD, JON, ØVERLAND, MARGARETH, HUGHES, ADAM D. & STANLEY, MICHELE 2019 The Environmental Risks Associated With the Development of Seaweed Farming in Europe - Prioritizing Key Knowledge Gaps. *Frontiers in Marine Science* **6**.
- CANDELIER, FABIEN, BOYER, FREDERIC & LEROYER, ALBAN 2011 Three-dimensional extension of Lighthill's large-amplitude elongated-body theory of fish locomotion. *Journal of Fluid Mechanics* **674**, 196–226.
- CARRINGTON, EMILY 1990 Drag and dislodgment of an intertidal macroalga: consequences of morphological variation in *Mastocarpus papillatus* Kützting. *Journal of Experimental Marine Biology and Ecology* **139** (3), 185–200.
- FREDRIKSSON, DAVID W., DEWHURST, TOBIAS, DRACH, ANDREW, BEAVER, WILLIAM, GELAIS, ADAM T. ST., JOHNDROW, KATHRYN & COSTA-PIERCE, BARRY A. 2020 Hydrodynamic characteristics of a full-scale kelp model for aquaculture applications. *Aquacultural Engineering* **90**, 102086.
- GOSSELIN, FRÉDÉRIK, LANGRE, EMMANUEL DE & MACHADO-ALMEIDA, BRUNO A. 2010 Drag reduction of flexible plates by reconfiguration. *Journal of Fluid Mechanics* **650**, 319–341.
- GREBE, GRETCHEN S., BYRON, CARRIE J., GELAIS, ADAM ST., KOTOWICZ, DAWN M. & OLSON, TOLLEF K. 2019 An ecosystem approach to kelp aquaculture in the Americas and Europe. *Aquaculture Reports* **15**, 100215.
- HENRIQUEZ, S. & BARRERO-GIL, A. 2014 Reconfiguration of flexible plates in sheared flow. *Mechanics Research Communications* **62**, 1–4.
- JACOBSEN, NIELS G., BAKKER, WOUT, UIJTTEWAAL, WIM S. J. & UITTENBOGAARD, ROB 2019 Experimental investigation of the wave-induced motion of and force distribution along a flexible stem. *Journal of Fluid Mechanics* **880**, 1036–1069.
- JOHNSON, AMY S. 2001 Drag, drafting, and mechanical interactions in canopies of the red alga *Chondrus crispus*. *The Biological Bulletin* **201** (2), 126–135.
- KOBAYASHI, NOBUHISA, RAICHLER, ANDREW W. & ASANO, TOSHIYUKI 1993 Wave Attenuation by Vegetation. *Journal of Waterway, Port, Coastal, and Ocean Engineering* **119** (1), 30–48.
- LECLERCQ, TRISTAN & DE LANGRE, EMMANUEL 2018 Reconfiguration of elastic blades in oscillatory flow. *Journal of Fluid Mechanics* **838**, 606–630.
- LECLERCQ, T., PEAKE, N. & DE LANGRE, E. 2018 Does flutter prevent drag reduction by reconfiguration? *Proceedings of the Royal Society A: Mathematical, Physical and Engineering Sciences* **474** (2209), 20170678.
- LEI, JIARUI, FAN, DIXIA, ANGERA, ANDREA, LIU, YUMING & NEPF, HEIDI 2021 Drag force and reconfiguration of cultivated *Saccharina latissima* in current. *Aquacultural Engineering* **94**, 102169.
- LEI, JIARUI & NEPF, HEIDI 2019a Blade dynamics in combined waves and current. *Journal of Fluids and Structures* **87**, 137–149.
- LEI, JIARUI & NEPF, HEIDI 2019b Wave damping by flexible vegetation: Connecting individual blade dynamics to the meadow scale. *Coastal Engineering* **147**, 138–148.
- LIGHTHILL, MICHAEL JAMES 1971 Large-amplitude elongated-body theory of fish locomotion. *Proceedings of the Royal Society of London. Series B. Biological Sciences* **179** (1055), 125–138.
- LUHAR, M., INFANTES, E. & NEPF, H. 2017 Seagrass blade motion under waves and its impact on wave decay. *Journal of Geophysical Research: Oceans* **122** (5), 3736–3752.
- LUHAR, M. & NEPF, H.M. 2016 Wave-induced dynamics of flexible blades. *Journal of Fluids and Structures* **61**, 20–41.
- LUHAR, MITUL & NEPF, HEIDI M. 2011 Flow-induced reconfiguration of buoyant and flexible aquatic vegetation. *Limnology and Oceanography* **56** (6), 2003–2017.
- PAIDOUSSIS, MICHAEL P. 1998 *Fluid-Structure Interactions: Slender Structures and Axial Flow*. Academic Press.

- PEIRCE, F. T. 1930 26—the “Handle” of Cloth as a Measurable Quantity. *Journal of the Textile Institute Transactions* **21** (9), T377–T416.
- STUDENT 1908 The Probable Error of a Mean. *Biometrika* **6** (1), 1–25.
- SUN, HONGWEI, YOU, YUNXIANG & LEI, JIARUI 2024 Deflection and drag on flexible marine structures in steady currents and internal solitary waves. *Physics of Fluids* **36** (10), 106603.
- VETTORI, DAVIDE, PEZZUTTO, PAOLO, BOUMA, TJEERD J., SHAHMOHAMMADI, AMIRARSALAN & MANES, COSTANTINO 2024 On the wave attenuation properties of seagrass meadows. *Coastal Engineering* **189**, 104472.
- VOGEL, STEVEN 1989 Drag and Reconfiguration of Broad Leaves in High Winds. *Journal of Experimental Botany* **40** (217), 941–948.
- VOGEL, STEVEN 1996 *Life in Moving Fluids: The Physical Biology of Flow*, 2nd edn. Princeton, NJ: Princeton University Press.
- WEI, ZHILONG, SHAO, YANLIN, KRISTIANSEN, TRYGVE & KRISTIANSEN, DAVID 2024 An efficient numerical solver for highly compliant slender structures in waves: Application to marine vegetation. *Journal of Fluids and Structures* **129**, 104170.
- WHITTAKER, PETER, WILSON, CATHERINE A. M. E. & ABERLE, JOCHEN 2015 An improved Cauchy number approach for predicting the drag and reconfiguration of flexible vegetation. *Advances in Water Resources* **83**, 28–35.
- ZHU, LONGHUAN, LEI, JIARUI, HUGUENARD, KIMBERLY & FREDRIKSSON, DAVID W. 2021 Wave attenuation by suspended canopies with cultivated kelp (*Saccharina latissima*). *Coastal Engineering* **168**, 103947.